Materials Characterization 224 (2025) 115050

Contents lists available at ScienceDirect

Materials Characterization

journal homepage: www.elsevier.com/locate/matchar

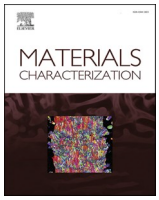

Microstructural analysis of tungsten single crystals irradiated by MeV W ions: The effect of irradiation dose and temperature

J. Zavašnik [a,b,*], A. Šestan [a,b], T. Schwarz-Selinger [c], K. Hunger [c], E. Lu [d], F. Tuomisto [d], K. Nordlund [d], E. Punzón-Quijorna [a], M. Kelemen [a], J. Predrag [a], M.L. Crespillo [e], G. García López [e], P. Zhang [f], X. Cao [f], S. Markelj [a,**]

[a] Jožef Stefan Institute, Jamova cesta 39, 1000 Ljubljana, Slovenia
[b] Max-Planck-Institut für Nachhaltige Materialien, Max-Planck-Str. 1, 40237 Düsseldorf, Germany
[c] Max-Planck-Institut für Plasmaphysik (IPP), Garching, Germany
[d] Department of Physics, University of Helsinki, Helsinki, Finland
[e] Center for Micro Analysis of Materials (CMAM), Universidad Autónoma de Madrid (UAM), Cantoblanco, 28049 Madrid, Spain
[f] Institute of High Energy Physics, Chinese Academy of Science, 100049 Beijing, China

ARTICLE INFO

Keywords:
Tungsten
Heavy-ion irradiation
Structural defects
SEM
TEM
PAS

ABSTRACT

We investigated the microstructural evolution of W(111) single crystals under high-energy self-ion irradiation at 290 K and 800 K, using complementary characterization techniques, including Scanning electron microscopy (SEM), Transmission electron microscopy (TEM), Rutherford backscattering spectrometry in channelling regime (RBS-C), Positron annihilation spectroscopy (PAS), and Nuclear reaction analysis (NRA). Irradiation with MeV W ions allowed for controlled defect formation, with dose and temperature significantly affecting defect type and distribution. At 290 K, interstitial defects evolved from dislocation loops at low doses (0.02 dpa) to dislocation networks at higher doses (0.2 dpa). In contrast, at 800 K, lower dislocation densities were observed, with nm-sized dots and isolated lines forming at 0.02 dpa and developing into longer dislocation lines (~30 nm) at 0.2 dpa. RBS-C spectra support these findings, showing a trend of increasing dislocation density with dose but decreasing with temperature. PAS analyses revealed mono-vacancies and small vacancy clusters (V_2–V_4) at 290 K, coalescing into larger clusters (V_{25}–V_{50}) at 800 K. NRA measurements indicated greater deuterium retention at 290 K than at 800 K, consistent with lower vacancy mobility at the lower temperature. Combined TEM, RBS-C, PAS, and NRA observations highlight increased vacancy mobility and defect recombination with temperature, forming larger vacancy clusters at 800 K. This comprehensive study provides quantitative insights into defect formation and evolution in W single crystals, presenting a comparative analysis of defect distributions across multiple techniques and revealing temperature-dependent mechanisms of microstructural change.

1. Introduction

Tungsten (W) has been selected as the primary material candidate for plasma-facing components in future fusion reactors due to its high melting point, excellent thermal conductivity, and low intrinsic hydrogen isotope (HI) retention. However, in the environment of a future fusion reactor, the 14 MeV neutrons generated from the deuterium–tritium fusion reaction will induce the formation of defects within the W crystal, altering its physical properties. Moreover, tungsten must withstand challenging reactor conditions, where damage formation at elevated temperatures, helium accumulation, and hydrogen retention will interact and mutually influence each other.

The displacement damage caused by neutrons can be well-replicated by high-energy ion irradiation, such as MeV W ions [1,2], but without transmutation, helium production and, most importantly, activation of the material. Neutron irradiation typically involves an initial impact on a W atom, creating a primary knock-on atom (PKA), which is then displaced with significant energy. The displaced W ion subsequently causes further displacement damage, accounting for the majority of the damage produced by neutron impact, and for which the W ion irradiation is a

* Corresponding author at: Jožef Stefan Institute, Jamova cesta 39, 1000 Ljubljana, Slovenia.
** Corresponding author.
E-mail addresses: janez.zavasnik@ijs.si (J. Zavašnik), sabina.markelj@ijs.si (S. Markelj).

https://doi.org/10.1016/j.matchar.2025.115050
Received 24 November 2024; Received in revised form 11 April 2025; Accepted 14 April 2025
Available online 15 April 2025

good proxy. In the context of heavy ion or neutron irradiation, displacement damage refers to the displacement of lattice atoms from their equilibrium positions, leading to the creation of lattice defects such as vacancies, self-interstitials, vacancy clusters, voids, and dislocation lines or loops. Open-volume defects act as trapping sites with high detrapping energy for hydrogen isotopes [3], which can increase fuel retention within the materials in future fusion reactors [4].

Given the significant impact of irradiation-induced defects on material properties, precise analytical methodologies are essential for studying these changes under varying irradiation conditions. Numerous studies have focused on defect creation in tungsten, examining how these defects evolve with temperature and under different irradiation conditions [4–6]. Experimental evidence suggests that the saturation of radiation-induced defects occurs at approximately 0.1–0.2 dpa, as determined by techniques such as hydrogen isotope retention [5–7], Transmission Electron Microscopy (TEM), Positron Annihilation Spectroscopy (PAS) [7–9], and by thermal diffusivity measurements using transient grating spectroscopy [10]. These findings are further supported by theoretical work employing Molecular Dynamics (MD) simulations based on the creation-relaxation algorithm (CRA) [10,11]. A recent comprehensive experimental investigation conducted by Wang et al. [7] showed that microstructure damage asymptotically reaches a steady-state and is expressed by a constant density and size of defects. Furthermore, above 0.1 dpa, the hardness no longer increases, and the deuterium retention saturates.

However, most of these studies have been conducted under room temperature irradiation conditions. In future fusion reactors, the 14 MeV neutron irradiation will occur at elevated temperatures, where the exact temperature depends on the cooling scenario and is estimated to be between 600 and 800 K [4,12,13]. Experiments at elevated temperatures, such as by Schwarz-Selinger [14], have studied damage dose dependence at 300 K and 800 K by deuterium retention and TEM microstructure analysis [15]. The studies of deuterium retention in samples irradiated at different elevated temperatures show that fewer defects are created when irradiations are performed at elevated temperatures [6,16,17] compared to when irradiation is conducted at room temperature, followed by annealing. On this topic, Yi et al. provided a detailed analysis of loop size as a function of the irradiation temperature (ranging from RT to 1073 K) and damage dose [18–20]. Further, Hu et al. [21] performed a TEM study of microstructure and the generation of open volume defects via PAS on samples irradiated at RT, 773 K, and 973 K. Their findings show that irradiation at room temperature predominantly results in single vacancies as detected by PAS. In contrast, irradiation at high temperatures leads to the formation of larger vacancy clusters, detectable by both PAS and TEM. Similarly, Jiang et al. [22] studied the effects of dose rate in self-ion irradiated monocrystalline and polycrystalline tungsten at 900 K up to 1 dpa using Rutherford Backscattering Spectrometry in Channelling mode (RBS-C). RBS-C enables the quantification of crystal structure disorder, which includes structural imperfections such as point defects, extended defects, distortions, etc., by measuring changes in the backscattered particle yield along a specific crystallographic direction [23]. Their study demonstrates that the dose rate influences the damage creation at 900 K.

The theoretical and modelling approaches are currently capable of simulating displacement-damaged tungsten [11,24,25]. However, the predictions are only valid for low-temperature irradiation conditions, typically below 500 K for tungsten, where vacancies are not mobile. In our previous study [26], we demonstrated how modelling results can be qualitatively compared with experimental results using microstructure outputs from molecular dynamics (MD) simulations of overlapping cascades as inputs for modelling RBS-C spectra using the RBSADEC code [27]. It was found that RBS-C is particularly sensitive to dislocation-type defects [27,28], and utilising different probing beam energies can provide additional and complementary information about defect structures that cannot be accessed through single-energy RBS-C measurements [26]. This method showed good agreement with samples irradiated at room temperature, but its validity at elevated temperatures is yet unknown.

The motivation for the current study is to investigate the influence of exposure temperature on defect formation in tungsten (W) single crystals using multiple analytical techniques. We analysed crystal lattice modifications induced by high-energy W ion irradiation at 290 and 800 K. Structural changes were assessed by electron microscopy, RBS-C [26], PAS, and deuterium retention using nuclear reaction analysis (NRA) [29]; the main experimental parameters are summarised in Table 1. Each technique provides complementary insights into the microstructure evolution: electron microscopy, with its high spatial resolution, enables visualisation of micro- and nanoscale defects; PAS is sensitive to single vacancies and vacancy clusters; and RBS-C allows for quantitative depth profiling of induced defects within the crystal lattice. Since hydrogen isotopes are trapped in W at open-volume defects, deuterium depth profiling by NRA can be used to determine both the depth distribution and total concentration of these defects. In combination with thermal desorption spectroscopy (TDS) and macroscopic rate equation modelling, we obtained information on the binding energies of hydrogen to specific defects and their concentrations [30].

Although RBS-C and NRA are generally considered non-destructive, precautions must be taken to minimize potential sample alterations. Specifically, excessive He implantation during analysis can introduce unintended damage or He as impurity. In our experiments, the ion fluence was carefully controlled to remain below the threshold for detectable damage, and the analysis positions were systematically shifting across the sample to prevent localized accumulation of irradiation effects. In the case of RBS-C, the applied He beam energy was high to ensure that most of the energy deposition occurred beyond the region containing irradiation-induced defects. For NRA, extensive deuterium depth profiling has demonstrated that up to two measurements can be performed on W-irradiated samples without any observable effect on D retention behaviour, and for repeated analyses shifting to a new measurement location on the sample is needed. It is important to note that the potential impact of multiple NRA analyses may vary for different materials, but such considerations fall beyond the scope of this study.

The investigation aims to understand the creation of defects and their interaction with hydrogen isotopes, in order to develop predictive models that can guide the design of materials with optimised properties for high-temperature, radiation-intensive environments. By extending our analysis to elevated temp eratures, we aim to explain how the defect landscape in tungsten evolves under conditions that more closely mimic those expected in future fusion reactors. Combining analysis methods capable of detecting different length scales offers a unique perspective by probing the material structure alterations resulting from high-energy ion irradiation.

2. Materials and methods

2.1. Analytical techniques

2.1.1. Electron microscopy

Micron-scale observation analyses were performed on a scanning

Table 1
Comparison of the applied research techniques in this study.

Order of experimentation	Technique	Information depth range	Likehood of destructive or not
1	SEM / ECP	~ 1 μm @ 30 kV	Non destructive
2	TEM (FIB)	~ 15 μm	Only locally destructive
3	PALS	~ 30 μm	Non destructive
4	PAS-DB	~ 0.5 μm	Non destructive
5	RBS-C	~ 4 μm	Non destructive
6	NRA	~ 7 μm	Non destructive
7	TDS	Whole sample	Destructive

electron microscope (SEM, Prisma-E, Thermo Fisher Scientific) operating at variable accelerating voltages in the range of 5–30 kV in high-vacuum mode ($< 6 \times 10^{-4}$ Pa), installed at Jožef Stefan Institute (JSI), Ljubljana, Slovenia. The backscattered electrons were collected by a lens-mounted solid-state annular segmented Directional Backscatter Detector (DBS, Thermo Fisher Scientific). Nano-scale observations and analyses were performed using a transmission electron microscope (S/TEM, ARM-200CF, JEOL Inc.) operating at 200 kV. The micrographs in scanning TEM mode were recorded by a dedicated bright-field (BF-STEM) detector. Thin samples for TEM analyses were produced following the site-specific focused ion beam method (FIB, Helios Nanolab 650i, Thermo Fisher Scientific) using Ga^+ ions. The sample surface was first protected by Pt deposit, followed by initial 30 keV ion milling with subsequent ion beam current reduction until electron transparency of the samples was achieved. Additional final polishing to reduce Ga^+ surface damage was done at 5 keV. The available information depth from such prepared samples is ~ 4 μm.

2.1.2. Positron annihilation spectroscopy – Lifetime and Doppler broadening

Positron annihilation spectroscopy is a non-destructive technique for investigation of atomic-sized open-volume defects in crystalline solids [31,32]. The implanted positrons lose kinetic energy very quickly (a few picoseconds) when entering the matrix by electron and phonon scattering. The annihilation process with electrons exhibits a specific lifetime, which depends on the electron density. Two γ phonons are then emitted in opposite directions with the energy of 511 ± ΔE keV, where ΔE is the Doppler shifting from 511 keV due to the electron momentum. The reduction of electron density at open-volume vacancy defects results in less probability of positron annihilation with high momentum core electrons than in the defect-free state. In this research, both positron annihilation lifetime spectroscopy (PALS) and positron annihilation Doppler broadening spectroscopy (PAS-DB) have been used to measure the as-annealed single crystal and post-irradiated samples.

PALS was performed at the University of Helsinki [33] with a digital coincidence lifetime spectrometer with a time resolution function of 155 ps (FWHM) [34]. A positron source (^{22}Na wrapped in 1.5 μm thick Al foil) was sandwiched between single crystal tungsten annealed at 2325 K and another sample with different irradiation conditions. In total, two million events are collected for each lifetime spectrum to guarantee the statistic. The lifetime spectrum was analysed as a sum of exponential decay components $n(t) = \sum_i I_i \exp(t/\tau_i)$ (with $\sum_i I_i = 1$) convoluted with the Gaussian resolution function of the spectrometer. To proceed the component analysis of positron lifetimes in the irradiated sample, we firstly subtracted the annihilations in the source as 210 ps (10.41 %) and 400 ps (4.0 %). The background contribution as 1500 ps (~0.1 %) has been corrected as well. Additionally, we made a third correction from the spectra with 108 ps (42.5 %), which represents the annihilation signals in the annealed reference of sandwich by "half".

The PAS-DB measurements of positron annihilation radiation were performed on the reference and irradiated samples with a variable monoenergetic slow positron beam at the Institute of High Energy Physics (IHEP, CAS, China). Positron implantation energies varied from 0.2 to 20 keV, corresponding to a mean penetration depth of up to 0.27 μm (maximum information depth ~ 0.5 μm), which were estimated by the empirical formula $Z(E) = 40E^{1.62}/\rho$, with the density $\rho = 19.35\ \mathrm{g/cm^3}$. A high-resolution Doppler broadening spectrometer coupled with a high-purity germanium (HPGe) detector (energy resolution of 1.25 keV at 511 keV) was utilised for the Doppler broadening recordings. The line-shape parameters, *S* and *W*, are integrated from the Doppler spectrum with the windows for electron momentum of the annihilating electron-positron pair. *S* represents to the fraction of positron annihilated with low momentum electrons (with momenta range $|P_L| < 0.4$ a.u.). *W* is associated with the annihilation occurs between positrons and high momentum electrons (in the momentum range 2.1 a.u. $< |P_L| <$ 4.14 a.u). More methodological details have been expressed in supplementary materials.

2.1.3. Rutherford backscattering spectrometry in channelling configuration (RBS-C)

RBS-C experiments were performed at the standard multipurpose line at the Centre for Micro Analysis of Materials (CMAM, UAM, Spain), with four ^{4}He beam energies [35]. The experimental chamber is equipped with a 3-axis rotation and variable height goniometer (Panmure Instruments, UK), allowing the precise orientation of the samples for RBS-C experiments (Fig. 1) with a maximum angle of 360° Phi, ± 75° Theta and ± 30° tilt with precision better than 0.01°. The goniometer is mounted on a table, allowing vertical movement (lift) up to 22 mm. The cylindrical sample holder is placed in the centre of the goniometer (in Fig. 1, a circular hole surrounded by the direction of phi rotation). The beam direction is along the X-axis, as shown in Fig. 1.

The experimental chamber is equipped with two silicon detectors (Ortec BU-012-050-500) for the detection of charged particles. One is fixed, and the other is mounted on a carousel, which allows for the variation of the scattering angle and installation of absorbent filters (Fig. 1). For our experiments, the fixed and mobile silicon detectors were used. The fixed detector was positioned at 170° relative to the incoming beam with a solid angle of $(4.1 \pm 0.1) \times 10^{-3}$ sr. The mobile detector was placed at 150° for complementary spectra verification.

2.1.4. Nuclear reaction analysis (NRA)

The experiment was performed at the 2 MV Tandetron accelerator in the INSIBA chamber [24,28] at Jožef Stefan Institute (JSI). The experimental set-up is schematically shown in [24]. The ^{3}He ion beam was oriented perpendicularly to the sample surface. Particles produced by the nuclear reaction are detected by a thick silicon detector (referred to as an NRA detector) with a depletion thickness of 1.5 mm. The detector has a circular aperture with a diameter of 19.54 mm and is positioned 104 mm from the target. The geometrical solid angle of the detector is 26.69 msr ± 0.12 msr. To stop the backscattered ^{3}He beam, a 24 μm thick Al absorber foil was placed in front of the NRA detector. The detector was positioned at a 160° angle relative to the incoming beam. The size of the beam spot on the target was defined by a circular orifice positioned in the beam line. We also employed another silicon detector for backscattered particles, the so-called Rutherford backscattering spectroscopy (RBS) detector, with a depletion thickness of 300 μm, located 135 mm from the target at 165° angle relative to the incoming beam, covering a geometrical solid angle of 0.7 msr ± 0.02 msr. The beam current was measured by an ion mesh charge collector with a tungsten mesh with 77.4 % geometrical transmission and bias on surrounding electrodes of −600 V [29]. To prevent channelling during the D depth profile analysis, the samples were tilted by 3 degrees and rotated by 6 degrees relative to the incoming ion beam. The D(^{3}He,p)^{4}He nuclear reaction [36] was used to analyse the retained deuterium with six different ^{3}He energies ranging from 730 keV to 4.3 MeV, with a 2 mm ^{3}He beam size. Absolute quantitative local information on the D concentration down to 7.2 μm was obtained by deconvoluting all measured proton energy spectra simultaneously using the software NRADC [37] and SIMNRA 6.02 [38]. For the 0.2 dpa/290 K sample, a single ^{3}He energy of 2.5 MeV was used to obtain the D depth profile, and the proton spectrum was then fitted using the SIMNRA program.

2.1.5. Thermal desorption spectroscopy (TDS)

The D desorption spectra from the samples were measured two months after the NRA analysis using thermal desorption spectroscopy (TDS), keeping the samples in a desiccator. The TDS measurement was performed in a quartz tube of the TESS set-up at IPP [39,40] using a tubular furnace. A 3 K/min linear heating ramp up to 1010 K and a > 30 min hold at the highest temperature was applied. The desorbed gases were measured with a Pfeiffer/Inficon DMM 422 quadrupole mass spectrometer (QMS). The 15 mass channels were recorded: $m/z = 1, 2, 3,$

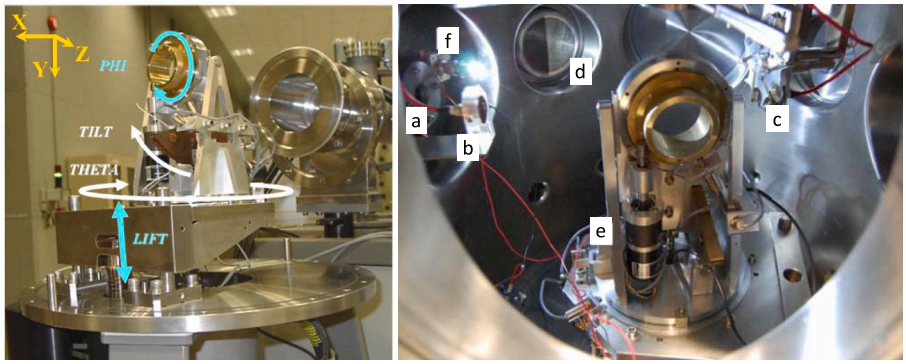

Fig. 1. (left) Picture of the goniometer with 3-axis of rotation (Theta, Tilt, Phi) and height (Lift) variable at the beam line. (right) Interior of the chamber: (a) entrance of the ion beam, (b) Si detector fixed at a scattering angle of 170°, (c) mobile Si detector, (d) gamma detector (Ge), (e) 3-axis goniometer, (f) light.

4, 12, 14, 16, 17, 18, 19, 20, 28, 32, 40, and 44. For the quantitative analysis, the QMS signal for D_2 was calibrated after each temperature ramp with a leak bottle from Laco Technologies with a flow of 1.22×10^{14} D_2/s and a stated accuracy of 4.6 %. The calibration factor for HD was determined by flowing HD through an orifice of known size from a calibrated volume of known absolute pressure (measured with a capacitance manometer and spinning rotor gauge) into the mass spectroscopy vessel. Based on the pressure recording of a calibrated spinning rotor gauge, the calibration factor for HD molecules per measured QMS count was 62 % of the one derived for D_2. To determine the amount of D desorbed during the measurement, masses 3 amu/q and 4 amu/q, corresponding to HD and D_2 molecules, respectively, were summed up.

2.2. Sample preparation

Single-crystal tungsten (W) samples with (111) orientation (purity 99.999 %) were obtained from Surface Preparation Laboratory B.V. The top surface was polished by the provider to a roughness Ra < 30 nm using chemical mechanical polishing (CMP) with colloidal silica with particles just below 100 nm in size. The residual subsurface deformation was monitored by Laue diffraction using 25 keV X-rays (white light with a 2D detector) and the samples were processed until no deformation-induced diffuse background and peak broadening was detectable.

The quality of the as-received SC(111) samples surface was evaluated by SEM with diffraction imaging at a zero-degree tilt, i.e. electron channelling pattern (ECP) imaging. The W samples were oriented parallel to the incoming electron beam at a working distance of 40 mm, and the ECP patterns were slow-scan recorded by solid state annular back-scattered (BS) lens-mounted directional detector capable of detection of electrons emitted at different angles. The channelling pattern is characteristic of the crystal lattice as the observed contrast originates from the interaction of the incident beam with lattice planes that are within a few degrees of the optical axis [41]. When the optical axis coincides with the direction of the local surface normal, the generated pattern represents the true orientation of the specimen, and the crystal orientation can be determined as the EC pattern is arising from known crystallographic planes.

The ECP patterns obtained on as-received SC(111) samples appeared

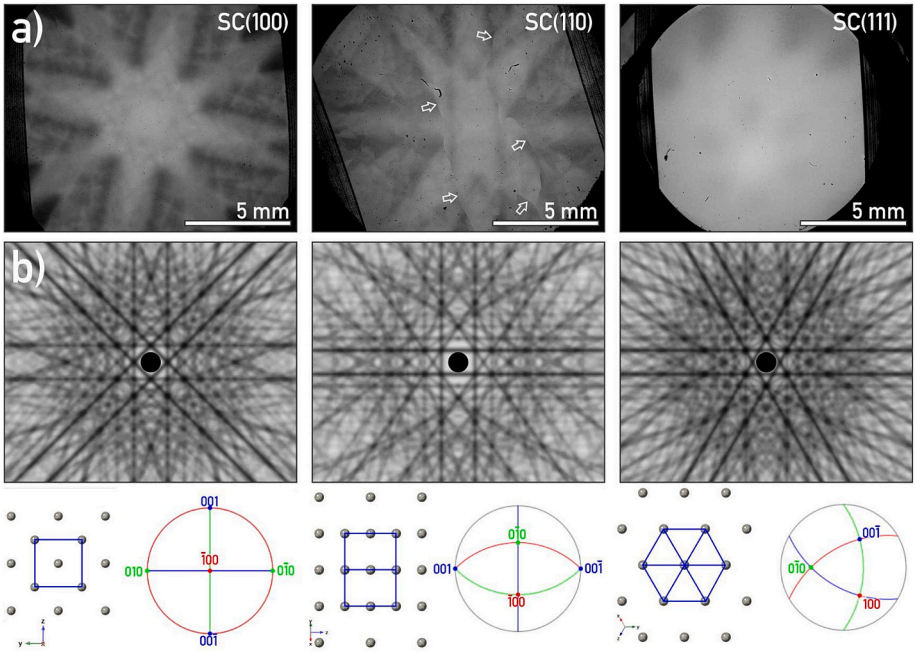

Fig. 2. (a) BSE channelling patterns of W single crystals (SC) in reference (100) and (110) orientation (arrows point to sub-grain boundaries, few black dust particles and fibres are seen attached on the surface), and as-received W sample in (111) orientation; back-scattered electron micrographs acquired at 30 kV, working distance 40 mm. (b) Simulated channelling patterns, with corresponding pole figures marked {010} green, {001} blue, and {100} red, and simulation of atom arrangement on the observed surface; unit cell marked blue. (For interpretation of the references to colour in this figure legend, the reader is referred to the web version of this article.)

more diffused than expected. For comparison and to establish a baseline, we mounted additional W(100) and W(110) single crystals in the same SEM stage. These reference samples were previously confirmed to have a well-ordered crystal structure and surface quality [42]. Under identical imaging conditions, the side-by-side comparison of all three samples allowed qualitative assessment of near-surface crystal structure damage (Fig. 2).

To assess the near-surface region, an accelerating voltage of 10 kV was used. According to Monte Carlo calculation, the penetration of primary electrons into W at 10 kV is up to 300 nm, with majority of the electrons stopping at <100 nm [43]. At these conditions, the ECP pattern for W(100) is well-formed and easily correlated with the simulated pattern. In the case of W(110), the pattern is partially disturbed by multiple low-angle grain boundaries, but still, we can clearly distinguish the main pattern features. For as-received W(111) sample, only a weak EC pattern was visible under the same conditions, indicating near-surface alterations of the crystal structure, reducing the electron channelling efficiency [41,44]. This plastically deformed layer can extend to a depth of 1–2 μm [45], potentially affecting ion channelling during the implantation process.

As original polishing procedure was not sufficient to obtain a defect-free microstructure, further surface treatment was necessary and the distorted layer was removed by chemo-mechanical vibration polishing at Max Planck Institute for Plasma Physics, Garching, Germany (IPP-Garching) by following procedure: grind up to P4000, polish for 1 h with 1 μm diamond suspension, follow with 1 h of 0.25 μm diamond suspension, with final polish with oxide polishing suspension (OPU Vibro, further details are summarised in *Supplementary Information File*). Afterwards, samples were annealed for 5 min at 2350 K in an ultra-high vacuum ($p < 5 \times 10^{-8}$ mbar) by electron beam heating, with slow ramps of less than 10 s/K for heat up and cool down to avoid defect creation by strain evolution or quenching. After polishing and annealing, the W single crystal samples showed a well-formed EC pattern, conforming to a well-ordered crystal structure without subgrains or other defects, as discussed below. Such samples were used in W ion irradiation experiments.

2.2.1. *Heavy-ion irradiation experiment*

After the surface preparation and annealing, the samples were irradiated with 10.8 MeV W^{4+} in the irradiation beam line at the 3 MV tandetron at IPP-Garching. Details of the setup and the sample holders for room temperature and high-temperature irradiation can be found in [14]. Samples were irradiated with a 7° tilt and rotated by 11° w.r.t the incoming beam. These angles were chosen in order to avoid channelling during irradiation and are based on the simulation calculations for mean ion range of 10 MeV W ions in W single crystal, shown in Fig. 3. The calculation is following the principles presented in [46]. The plot shows the mean projected ion range as a function of the polar and azimuthal incoming angle of the ion beam, with red and orange colours showing strong channelling, and blue negligible. While the calculation was conducted at a slightly different energy than in the experiments (10 MeV vs. 10.8 MeV), the angular dependence of channelling is expected to remain essentially the same. The calculation shows that we have strong axial channelling at ⟨111⟩, ⟨001⟩, ⟨011⟩, some at ⟨311⟩, and planar channelling between these directions. The channel widths are roughly 2 degrees for <001>, <011>, <311>, and roughly 3 degrees for <111>. The ion flux was continuously measured during the irradiation using Faraday cups located at four corners of a copper diaphragm in front of the sample holder. A focussed ion beam (2 mm FWHM) was raster scanned (1 kHz) across a square area, including the Faraday cups. The acquired ion fluence was determined from the size of the Faraday cups and the measured current over time.

Two irradiation temperatures (290 K and 800 K) and two damage doses (0.02 dpa and 0.2 dpa) were applied with the objective of creating four distinct types of dominant defects. The primary displacement-damaged zone in the W samples was simulated by SRIM 2008.04 code [47] using the 'Quick calculation of damage' option. A displacement energy of 90 eV and a surface binding energy of 0 eV was used. Results of SRIM simulation are shown in Fig. 3 for W fluence of 5.8×10^{12} W/cm^2 and predict a displacement-damaged zone in W extending down to 1.3 μm. We show the displacement depth profile in displacement per atom (dpa), the calculated displacements by recoils, direct ions and their sum, and the concentration of the implanted W ions. The "dpa" values were calculated by adding the "recoil" and "ion" displacements from the "vacancy.txt" output file and converting the sum by multiplying it with the ion fluence and dividing by the tungsten density. By this we get a depth profile of the number of displaced target atoms named as calculated displacements in "dpa". For the applied fluence of 5.8×10^{12} W/cm^2, the SRIM calculated number of displacements per ion and depth convert to a peak dose of 0.02 dpa at a depth of 0.6 μm (samples 78g/78c and 78h/78d) (Fig. 3). For ten-times-higher fluence, the peak damage dose is 0.2 dpa (samples 78f/78b, and 78a/78e). It should be noted that for irradiations at 800 K, SRIM damage depth profile calculation cannot be taken as a merit since vacancies become mobile in tungsten.

Irradiation temperatures of 290 and 800 K were selected, one being well below and one well above the temperature of 550 K, where vacancies in tungsten become mobile [33]. A low damage dose of 0.02 dpa was chosen in one case, being in the linear damaging regime. As the second damage dose, 0.2 dpa was selected, which is in the so-called high-damage limit where damage is known to saturate at low temperatures [11]. An overview of the damaging parameters and expected dominant damage type is given in Table 2.

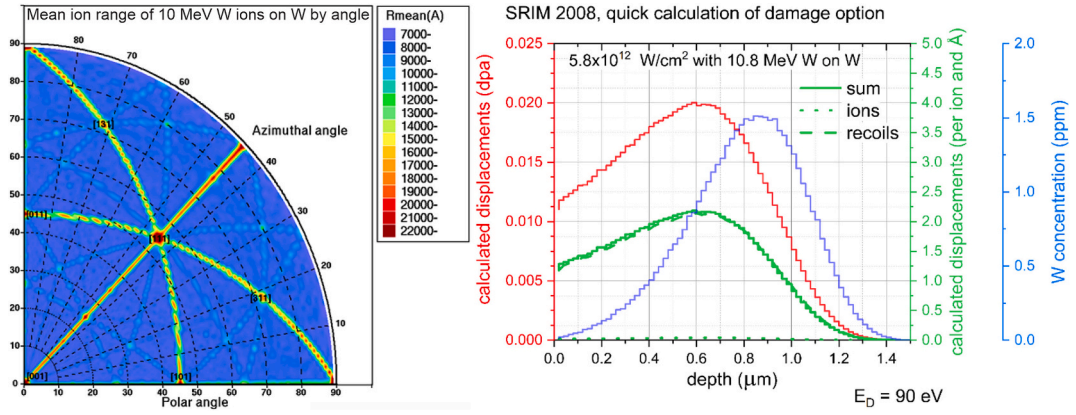

Fig. 3. (left) Calculation of the channelling map for 10 MeV W ions on tungsten single crystal. (right) SRIM calculated primary displacements created by the 10.8 MeV W ions, the W recoils and their sum (green axis and lines), the corresponding damage dose profile (red axis and line) and the concentration profile of the implanted W ions (blue axis and line) for the case of a W fluence of 5.8×10^{12} W/cm^2.

Table 2
Sample classification.

	Sample ID	Damage dose/temperature	Expected defects
1)	78f / 78a	0.2 dpa / 290 K	'Heavily damaged' [40,48]
2)	78b / 78e	0.2 dpa / 800 K	'Big vacancy clusters' [22]
3)	78g / 78h	0.02 dpa / 290 K	'Single vacancies' [21]
4)	78c / 78d	0.02 dpa / 800 K	'Small vacancy clusters' [21]

Two identical sets of samples were prepared: one for electron and ion beam analysis using RBS-C (78b,c,f,g) and the other for PALS, DB-PAS and D retention analysis (78a,d,e,h). The prediction of open volume defect formation is based on previous studies [21], where single vacancies were found to form at low doses during room temperature W ion irradiation, while small [21] or large [22] vacancy clusters dominated at different damage doses during W ion irradiation at 800 K. For samples 78g/78h (0.02 dpa), the average damage rate was 1.0×10^{-4} dpa/s, and for samples 78f/78a (0.2 dpa) 1.2×10^{-4} dpa/s, with peak damage rates being two orders of magnitude higher. To create an internal standard, sample 78 g was partially covered during W ion irradiation to preserve a defect-free crystal structure.

The second set of W-ion irradiated tungsten single crystal samples were, after the PAS analysis, additionally exposed to a plasma at 370 K with a D ion energy of 5 eV/D and a D-ion flux of 6×10^{19} D/m^{2}s for 48 h, resulting in a D ion fluence of 1×10^{25} D/m^2. The exposure was performed on a PLaQ plasma device at IPP-Garching. From previous experience, this fluence is sufficient to populate the defects with deuterium throughout the whole damage depth [5]. These samples were then used to analyse the D depth profile using ^{3}He NRA.

3. Results and discussion

3.1. Electron microscopy analyses (SEM, TEM)

3.1.1. Qualitative observation of the irradiation-induced structural damage by SEM

For crystalline materials, the BSE contrast is modulated by a dependence of the backscattered electron intensity on the orientation of the crystal lattice with respect to the primary beam direction [49]. When the incident electron beam satisfies the Bragg condition, the intensity of backscattered electrons (BSE) decreases, producing a distinct pattern that reflects changes in the beam's incidence direction [50,51].

The maximum damage depth in our W(111) sample, according to

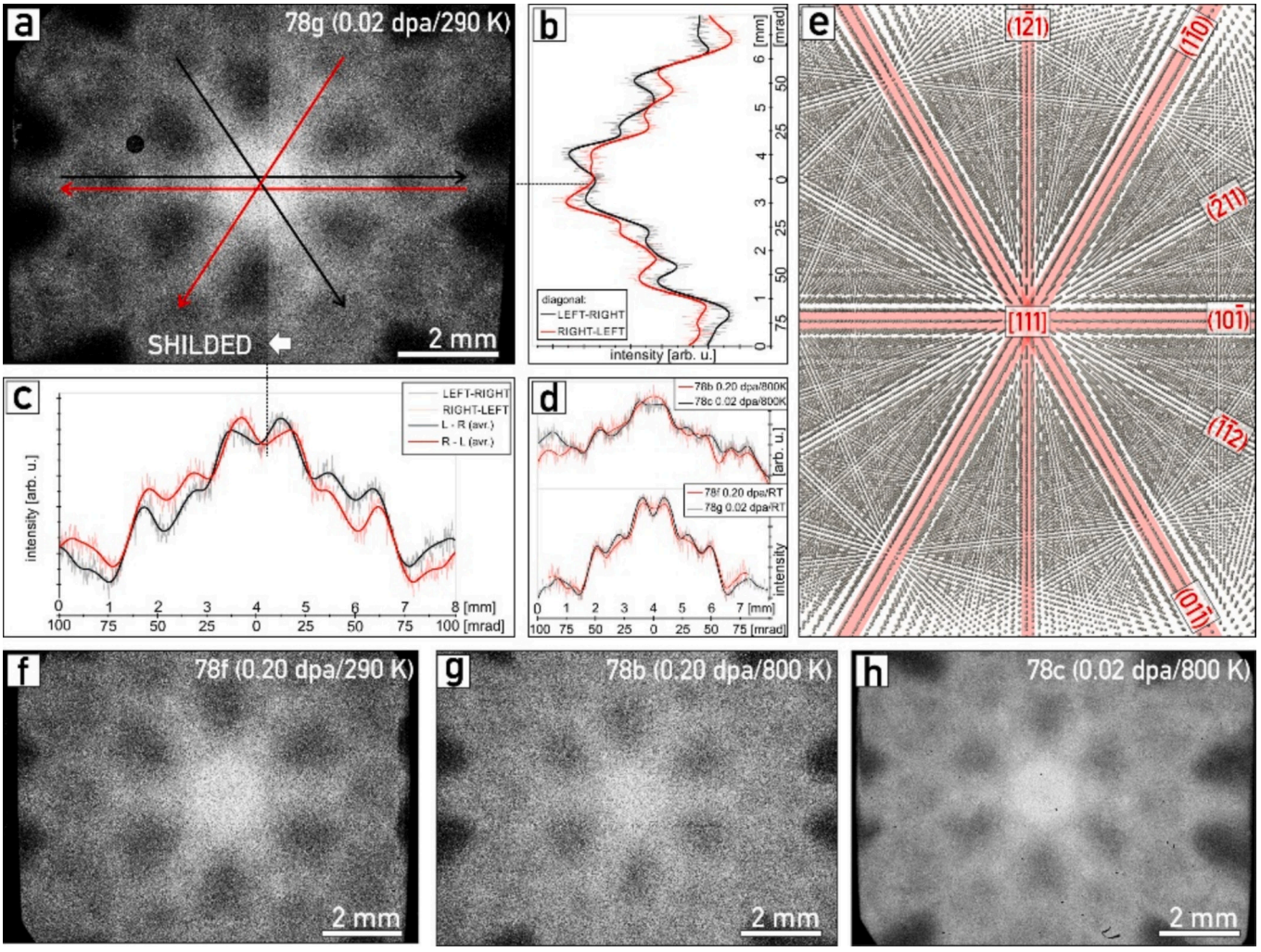

Fig. 4. (a) Electron channelling pattern (ECP) of sample 78g (0.02 dpa at 290 K), which was half-shielded during irradiation to serve as an internal standard. The white arrow indicates the boundary between the irradiated and shielded region. Coloured arrows correspond to (b) intensity profiles along diagonal (1−10) and (01−1) planes, and (c) intensity profiles along the (10−1) direction, showing differences in BSE yield between irradiated and unirradiated regions due to crystal structure defects. (d) Comparison of ECP intensity profiles from samples irradiated at 290 K and 800 K, for 0.20 and 0.02 dpa doses, showing temperature- and dose-dependent contrast changes. The intensities were extracted from (f–h) ECPs of samples irradiated to different doses and temperatures, from (10–1) plane. (e) Schematic projection of the tungsten crystal structure viewed along the [111] zone axis, with marked principal channelling directions.

SRIM (Fig. 3), is expected at ~0.5 μm. To access this region, we used an accelerating voltage of 30 kV. According to Monte Carlo simulation [43], at this voltage the estimated electron channelling information depth is up to 1 μm, with the majority of electrons stopping at approximately 0.5 μm (calculation in *Supporting Information File*). After recording the micrographs, we used the image-correlation method to measure the intensity of the main BSE bands in the W reference and the W-ion irradiated samples, where the changes were induced due to displacements in regions of interest [52].

The quantitative comparison of the channelling yield was assessed from sample 78g (0.02 dpa/290 K), using the non-irradiated half as internal W reference (Fig. 4a), and from there extracted intensity profiles shown in Fig. 4b. The deconvoluted intensity profile shows a ~ 5 % intensity decrease of the primary central peak, where the channelling effect is strongest (comparison of red and black intensity profile, Fig. 4b), and a 2.4 % increase of the (0−11) Kikuchi band width in the irradiated part of the sample 78g (Fig. 4c). Even without the internal standard, a decrease in peak intensity and an increase in peak width between samples irradiated at 290 K and 800 K can be observed due to different defect populations at a given temperature (Fig. 4d).

3.1.2. *Quantitative observation of the irradiation-induced structural damage by TEM*

The samples for scanning TEM analyses were prepared by FIB. In W monocrystal samples, the surface orientation is fixed to normal (111). The azimuthal orientation was determined from the EC pattern, and the lamella was cut parallel to the (010) plane, allowing the observation of the sample in the [1–10] zone axis. To establish a baseline, reference sample 78SC was polished and analysed in parallel (Fig. 5).

Bright-field scanning transmission electron microscopy (BF-STEM) was used to visualise the damage zone and determine the irradiation-induced defects. The depth of structural damage, i.e. deviation from a perfect lattice, was estimated from the averaged intensity profile obtained from BF-STEM images (Figs. 6, 7). Several factors may contribute to the observed contrast change, such as sample thickness, FIB etching rates, and the overall number of defects. To minimize artefacts affecting the contrast, the samples were prepared under the same conditions. The maximum depth of the observed damage zone closely matches the damage depths predicted by SRIM simulations; the depth primarily depends on the irradiation dose and is less influenced by temperature. For samples exposed to 0.2 dpa, the damage zone depth is 1.1 μm for both 290 K and 800 K irradiation (Fig. 6), while for 0.02 dpa samples, the damage zone depth increases from 0.7 μm at 290 K to 0.8 μm at 800 K (Fig. 7).

We observed a few nanometers thick zone in the near-surface region with fewer or no visible defects. When the dose increases from 0.02 dpa to 0.2 dpa, the thickness of this defect-free zone grows by a factor of 4. However, raising the irradiation temperature from 290 K to 800 K reduces the thickness of the zone by about half. For instance, at 290 K, the thickness increases from 10 nm at 0.02 dpa to 40 nm at 0.2 dpa, while at 800 K, it increases from 6 nm at 0.02 dpa to 25 nm at 0.2 dpa (see Table 3, and the *Supplementary Information File* for details).

In all samples, the dislocation density (ρ_d) in the first 100 nm section is lower than in the bulk, which we attribute to surface effects, where defects are mitigated at the free surface due to the absence of grain boundaries. For samples irradiated at 290 K, the ρ_d in the first 700 nm is slowly decreasing, with a constant number of loops and an increasing number of lines, stabilising at ~500 nm deep (Fig. 8a,b, data after Ref. [26]). For samples irradiated at 800 K, the ρ_d is almost constant for low-dose sample 78c (0.02 dpa/800 K) but gradually increases until the local maximum at 400–500 nm deep for 78b (0.2 dpa/800 K) sample (Fig. 8c). The number of loops and lines is more descriptive: for both samples, the number of lines gradually decreases from the surface, with one local maximum of 500 nm deep, while the number of loops increases with depth and reaches a maximum at 400 nm for both samples irradiated at 800 K (Fig. 8d).

A detailed TEM defect analysis and discussion of the samples irradiated at 290 K is summarised in [26]. It shows that under low dpa/290 K irradiation, dislocation loops are the dominant defects visible [7,53], while at higher dpa, numerous dislocation lines replace the loops as the primary visible defects [7,48]. For sample 78c, irradiated at 0.02 dpa/800 K, mainly nm-sized dots and several isolated lines (< 50 nm, in <111> direction) were observed. However, increasing dpa to 0.2 (sample 78b), dislocation lines form a square polygon with edges in <111> direction, approx. 30 nm long. The average dislocation density ρ_d for samples irradiated at 800 K is 1.07×10^{14} m/m^3 for sample 78b (0.2 dpa/800 K) and 1.05×10^{14} m/m^3 for sample 78c (0.02 dpa/800 K). The average dislocation density for samples irradiated at 290 K is more than a factor of two higher, being 2.21×10^{14} m/m^3 for sample 78f (0.2 dpa/290 K) and 2.75×10^{14} m/m^3 for sample 78g (0.02 dpa/290 K), In Table 3 we summarise the dislocation densities obtained on the studied samples and give a comparison to the literature data. The deviations in reported values can be attributed to different sample preparation methods (FIB, FIB+Ar/electropolishing, or electropolishing), different TEM defect detection techniques (conventional TEM or STEM [54]), and the non-uniform spatial distribution of defects, which is an intrinsic limitation of the line-intercept method [26,55]. In our work, we used the line-length method, and since all samples were prepared in the same orientation following the same protocol, post-treatment, and evaluation process, a qualitative comparison is possible.

At high damage doses and high temperatures, the observed dislocation structures can be compared to those reported by Chrominski et al. [15] and Ferroni et al. [56], where the dislocation structure closely resembles the one seen here for a high damage dose rate of 5×10^{-3} dpa/s in [15]. The dislocation density reported in [15] was 1.5×10^{14} m/m^3, which is in good agreement with the 0.2 dpa/800 K sample obtaining 1.07×10^{14} m/m^3. A detailed analysis of loop size in relation to irradiation temperature, ranging from room temperature to 1073 K, and damage dose was conducted by Yi et al. [18–20]. Similarly, Jiang et al. [22] studied the microstructure of tungsten samples irradiated at 1 dpa at 900 K, focusing on the distribution of void sizes. To the best of our knowledge, only the studies by Yi et al. [18] and Hu et al. [21] have investigated defects at low damage doses at 773 K, and a comparison of the dislocation density is given in Table 3.

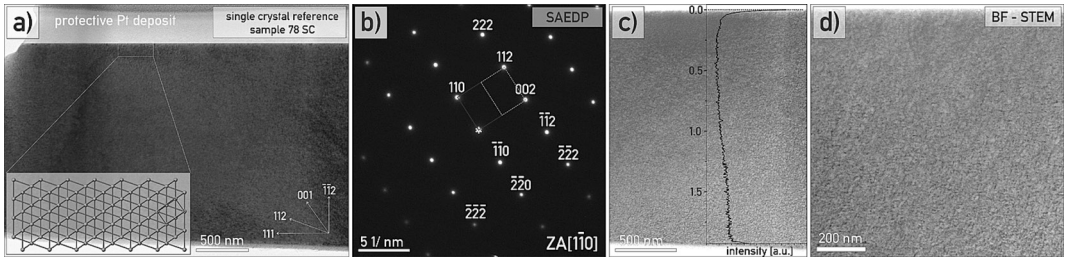

Fig. 5. (a) conventional TEM micrograph of reference sample 78SC, with marked principal lattice planes and atomic model of the zone axis view. (b) Corresponding selected-area electron diffraction pattern (SAEDP) indexed for W in [1–10] zone axis; blue square marks unit cell. (c) Overview BF-STEM micrograph with contrast intensity profile, and (d) near-surface BF-STEM micrograph.

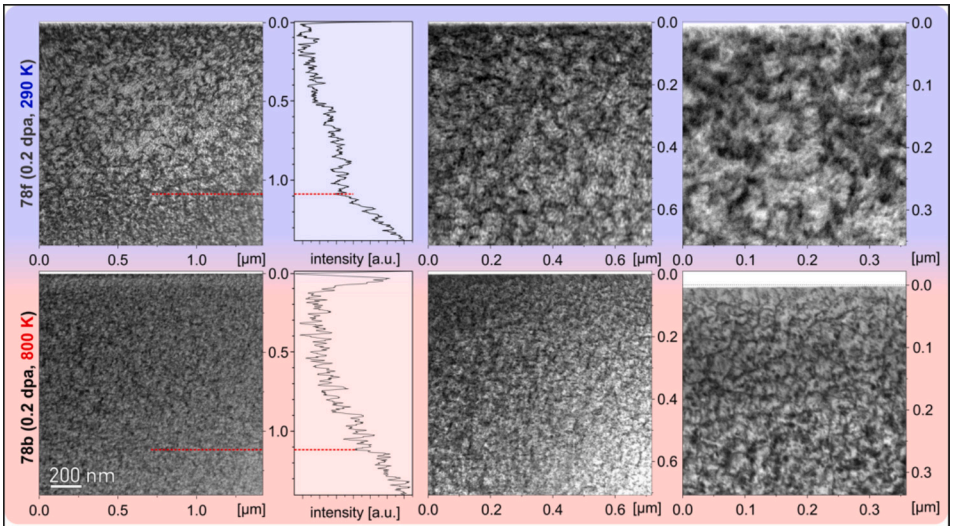

Fig. 6. BF-STEM micrographs for 0.2 dpa damaged samples irradiated at 290 K (78f) and 800 K (78b), with the magnified near-surface regions containing defects. The contrast intensity profile is aligned with the sample surface in the cross-section view; the maximum damage zone is marked with a red line. (For interpretation of the references to colour in this figure legend, the reader is referred to the web version of this article.)

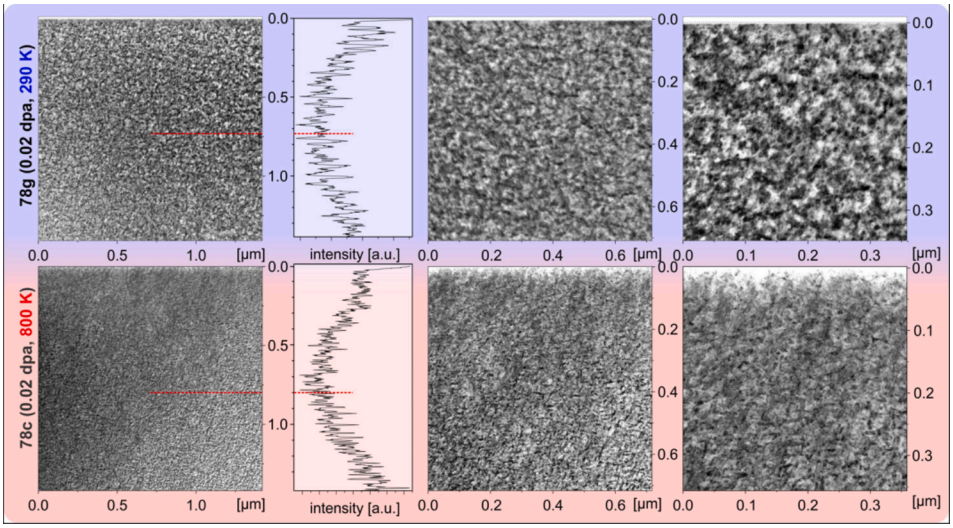

Fig. 7. BF-STEM micrographs for 0.02 dpa damaged samples irradiated at 290 K (78g) and 800 K (78c), with close-in on near-surface regions. The maximum damage zone is marked with a red line. (For interpretation of the references to colour in this figure legend, the reader is referred to the web version of this article.)

Initial TEM observations of the samples showed no signs of voids or cavities in the peak damage region. Similarly, Ferroni et al. [56] did not observe voids in tungsten irradiated to 1.5 dpa at 773 K; voids only became visible after annealing the samples for 1 h at 1073 K, where an average diameter of 1.5 nm was measured. In contrast, Hu et al. [21] observed cavities ranging from 0.97 to 1.13 nm in size, with densities between 1.65 and 1.73 $\times$ 10^{24} m^{-3}, in polycrystalline tungsten irradiated at 773 K with a dose of 0.02 dpa, though the damage mode was not specified. Similarly, Meng et al. [22] showed that for irradiation at 900 K, the average void diameter in single-crystal tungsten was 3.4 nm at a dose rate of 10^{-4} dpa/s and 2.4 nm at 10^{-3} dpa/s. The average void size in polycrystalline tungsten was approximately 40 % larger under the same conditions as in single-crystal W, increasing from 1.5 nm to 1.9 nm.

Considering this, we analysed sample 78b (0.2 dpa/800 K), where the largest voids were expected. At a depth of 750–1000 nm, below the peak damage depth of 600 nm (as calculated by SRIM), we found spherical features resembling voids, ranging in size from 0.25 nm to 1 nm (mean Feret diameter of 0.44 nm) with a density of 5.46 $\times$ 10^{24} m^{-3} (see *Supplementary Information file* for details). No such features were observed above or below this region, nor below 1 μm. The observed features are much smaller, and their density is much larger than reported by Hu et al. [21]. This discrepancy may be due to differences in damage rate or mode (in terms of depth) or can be related even to the TEM sample preparation process. In the cited studies, FIB lamellae were further electrochemically polished to remove residual FIB damage, potentially affecting void size through etching [57]. In contrast, our samples were finalised only by low-energy Ga ion milling.

3.2. Channelling Rutherford backscattering spectroscopy

The samples studied by TEM were also analysed by RBC-C. As presented in [26], the so-called multi-energy beam analysis method gives more detailed information about the type of defects and their extension. It is known that each type of ion-irradiation-produced defect has a particular influence on the analysing He beam depending on the energy (i.e., direct backscattering or enhanced dechannelling of the probing beam) [23,58]. For that purpose, we used four He beam energies: 4.5,

Table 3
Calculated dislocation density ρ_d (TEM line-length method) compared to reference values and maximum damage zone depth and thickness of the near-surface defect-depleted zone.

Sample	ρ_d [m/m^3]	ρ_d - reference values [m/m^3]	Max. damage zone depth [nm]	Near-surface defect depleted zone [nm]
78f 0.2 dpa/ 290 K	2.21×10^{14}	1.93×10^{14} [26] 2.3×10^{14} [7]	1100	40
78b 0.2 dpa/ 800 K	1.07×10^{14}	1.5×10^{14} (0.23 dpa) [15] 4.7×10^{14} (0.4 dpa) [19]	1100	25
78g 0.02 dpa/ 290 K	2.75×10^{14}	3.19×10^{14} [26] 1.68×10^{14} (0.05 dpa) [7]	700	10
78c 0.02 dpa/ 800 K	1.05×10^{14}	8.3×10^{13} (0.01 dpa) [18]	800	6

4.0, 3.5 and 3.0 MeV, impinging the samples along the <111> direction. Spectra obtained on all analysed samples at the four ^{4}He beam energies are shown in Fig. 9. The depth scale shown on the top axis is estimated based on the stopping power from SRIM in amorphous tungsten with surface energy approximation [59]. The channelling spectrum obtained on the non-irradiated half of the sample 78g is called "Pristine". The "Random" spectrum was obtained by adding 100 spectra collected for a combination of theta, tilt positions within a circle of a 3° angle radius around the <111> direction. The yield for the random orientation is the highest compared to the samples oriented in any channelling direction since it is considered as a non-aligned material with a considerable quantity of scattering centres. The pristine sample shows the lowest yield for the channelling direction; both spectra are shown in [26]. The samples W-irradiated at different damage doses and temperatures show an increase in the backscattered yield with the damage dose. For higher irradiation temperature, the yield is lower. The lowest yield is obtained on the sample 78c (0.02 dpa / 800 K), followed by samples 78g (0.02 dpa/290 K), 78b (0.2 dpa/800 K), and 78f (0.2 dpa/290 K). In the RBS spectra, one can also observe a change in the slope. This is the so-called 'knee point', where the initial high-energy yield arises from channelled ions backscattered directly from displaced atoms in the sample. Subsequently, the signal changes due to dechannelling, as previously discussed for the 290 K case in [26]. However, this change in the slope is barely noticeable on samples irradiated at 800 *K. no* distinct transition between the damage and dechannelling region was observed in [22] for samples irradiated at 900 K to 1 dpa. In the case of 290 K samples we previously discussed in [26] that the knee point depth is approximately 1.2 μm and 0.8 μm for 0.2 and 0.02 dpa damaged samples, respectively, showing good agreement with the TEM results. For the 800 K samples, however, this correlation is less straightforward. In the spectrum obtained with a 4 MeV He beam on sample 78b (0.2 dpa/800 K), a slight change in the slope is observed around 1.3 μm. However, no slope change is seen for sample 78c (0.02 dpa/800 K). Interestingly, for sample 78b (0.2 dpa / 800 K), the backscattering yield is lower at shallower depths compared to sample 78g (0.02 dpa/290 K), but at a depth of about 1.2 μm, the backscattering yield becomes higher. The

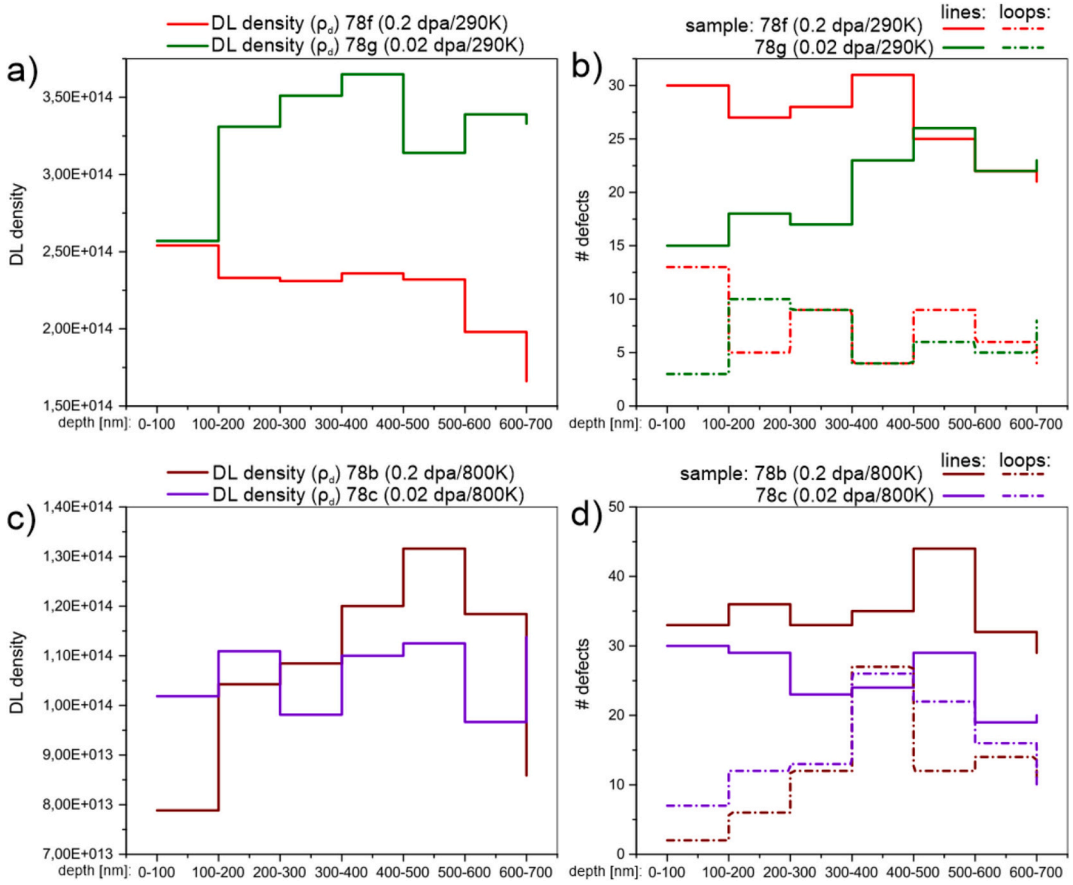

Fig. 8. Depth distribution of the dislocation density (ρ_d) for samples irradiated at 290 K (a) 78f (0.2 dpa/290 K) and 78g (0.02 dpa/290 K), and (b) ρ_d for 800 K irradiates samples 78b (0.2 dpa/800 K) and 78c (0.02 dpa/290 K). In parallel, the depth distribution of the total number of defects (#, loops and lines) for the same sets of samples at (c) 290 K and (d) 800 K irradiated samples.

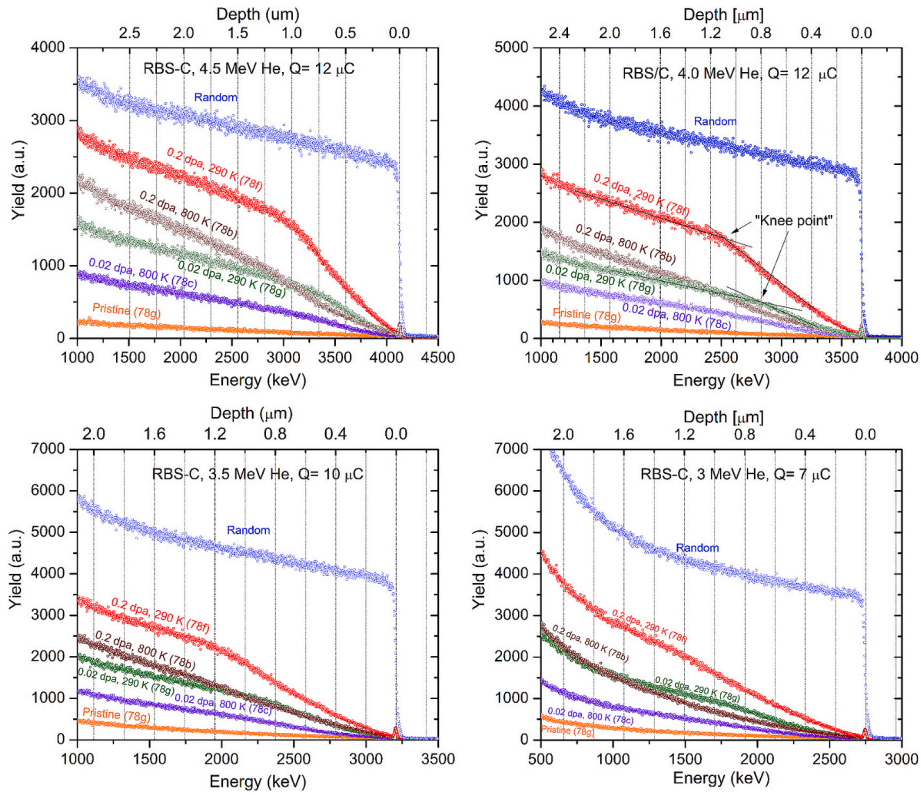

Fig. 9. RBS-C spectra in <111> channelling direction obtained with ^{4}He at 4.5, 4.0, 3.5 and 3.0 MeV at 170° scattering angle. The upper scale was derived by assuming SRIM stopping in amorphous material with surface energy approximation. "Pristine" is the channelling spectrum obtained on the non-irradiated sample, and "Random" spectrum was obtained by adding 100 spectra collected for a combination of theta, tilt positions around the <111> direction. On upper right graph we mark the "Knee point" position.

RBS-C spectra for the 0.02 dpa/800 K sample closely resemble the pristine spectra within the first 200 nm from the surface, suggesting minimal defect presence. This observation is also partially visible on the STEM micrographs (Fig. 7), where the grey structure within this region appears similar to the structure beyond a depth of 0.8 μm.

To estimate the irradiation-induced defects, we can calculate the relative disorder factor, f_d, by comparing the yield of each modified sample to that of the random and pristine samples. The f_d is calculated according to Eq. (1), where y_a is the spectrum yield for each irradiated sample, y_p is the spectrum yield for the pristine sample, and y_r is the spectrum yield for the random sample:

$$f_d = \frac{y_a - y_p}{y_r - y_p} \quad (1)$$

The values of relative disorder for the W-irradiated samples measured at the different beam energies are plotted in Fig. 10. They are calculated at a depth of 0.6 μm, where the damage peak maximum is located according to the SRIM calculation. According to the theory [23], the response of the induced structural damage signal versus analysing energy provides relevant information about the extension of the defects. The response is evaluated considering the slope of the curve "disorder factor vs beam energy". When the slope is negative, the material contains uncorrelated displaced lattice atoms (interstitials, vacancies or amorphous clusters). If the slope is zero, the material comprises extended defects (dislocation loops or dislocation lines), but they are not dominant. If the slope is positive, the predominant defects are extended defects (dislocation loops or dislocation lines).

We can observe that sample 78f (0.2 dpa/290 K, red data) has a positive slope. The sample 78g (0.02 dpa/290 K, green data), the sample 78b (0.2 dpa/800 K, brown data), and the sample 78c (0.02 dpa/800 K, purple data) show no slope. Considering the theory, the sample 78f (0.2 dpa/290 K, red data) with a positive slope would present extended defects as the predominant defect type.

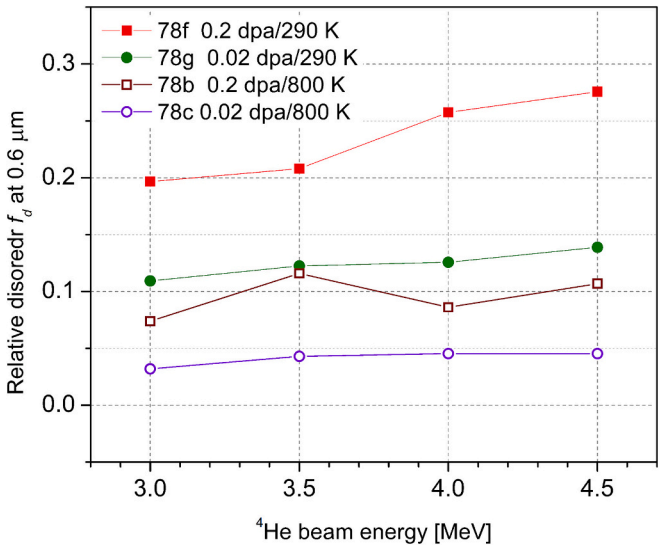

Fig. 10. Relative disorder versus energy for the four modified samples at a depth of 0.6 μm, where the damage peak maximum is located according to SRIM simulations. The lines are only to guide the eye.

Besides the relative disorder factor f_d, another parameter that can be measured and compared is the half-angle $\psi_{1/2}$, which defines the width of the channel. $\psi_{1/2}$ is defined as the angular half-angle of the yield profile at the yield value halfway between the minimum yield and the yield for random incidence [59]. In order to obtain the value experimentally, the backscattering yield is measured for a narrow window of

200 channels, just after the surface peak, while the sample is moved along the theta direction. Fig. 11 represents the theta scans for the pristine sample at four different He beam energies (4.5, 4, 3.5, and 3 MeV) around the <111> axial channel. The yield for the random incidence was normalised to 1 for comparison of the spectra. As it is expected from the equations described below, the dependence of $\psi_{1/2}$ with beam energy is inversely proportional to the square root of the energy. The values obtained from the graph are listed in Table 4.

Calculation of the half-angle has been performed considering the following equations, where Barrett's treatment is considered [59], and the expression for the half-angle can be written in degrees as:

$$\psi_{1/2} = 0.8 F_{RS}(\xi)\psi_1 \quad (2)$$

where the value of $F_{RS}(\xi)$ is obtained from Fig. 8.9 in [59], and ψ_1 is the characteristic angle, given by Eq. (3):

$$\psi_1 = 0.307(Z_1 Z_2 / Ed)^{1/2} \quad (3)$$

Here, Z_1 and Z_2 are the atomic numbers for the projectile and target atoms, respectively (Z_1(He) = 2 and Z_2(W) = 74), E is the beam energy in MeV and d is the interatomic spacing along <111> axial direction which is 2.74 Å for W [59]. The value for the normalised distance ξ, is given by the following expression where u_1 is the one-dimensional root mean square thermal amplitude (0.050 Å at 293 K for W):

$$\xi = \frac{1.2u_1}{a} \quad (4)$$

For our condition ξ equals 0.6, which then gives $F_{RS}(\xi)$ of 1.0. The Thomas-Fermi screening radius a is described by the following Eq. (5), where a_0 is the Bohr radius, a_0 = 0.528 Å, and

$$a = 0.8853 a_0 \left[\sqrt{Z_1} + \sqrt{Z_2}\right]^{\frac{-2}{3}} \quad (5)$$

The calculated values for different ^{4}He beam energies, as summarised in Table 4, are consistently slightly lower than the experimental results across all beam energies. For the higher ^{4}He energies, the calculated and experimental values agree within the error bars. However, at the two lowest ^{4}He energies, the experimental values are larger than the theoretical predictions.

For comparison, the linear scan along the <111> axial channel on the pristine sample has been simulated using the RBSADEC code [26,27] for a 4 MeV He beam and compared with the experimental RBS-C scan (see *Supporting Information File*). The agreement of the data shows the power of the RBSADEC code to simulate the RBS-C signal.

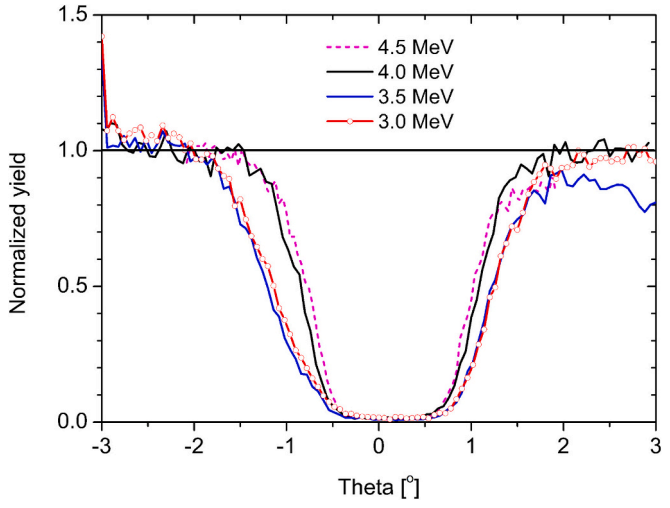

Fig. 11. Evolution of the channel width with the He bean energy for the pristine W(111) sample in <111> channelling direction.

Table 4
Values of experimental and calculated half angle $\psi_{1/2}$ for 4.5, 4, 3.5 and 3 MeV ^{4}He beam in <111> pristine tungsten.

E (MeV)	$(\psi_{1/2})_{experimental}$ (°)	$(\psi_{1/2})_{calculated}$ (°)
4.5	0.89 ± 0.05	0.85
4	0.96 ± 0.05	0.90
3.5	1.21 ± 0.05	0.96
3	1.21 ± 0.05	1.04

The evolution of the induced defects in the crystal lattice, influenced by the implantation conditions, can also be analysed through linear scans along the axial channel. The presence of defects in the crystal lattice influences the trajectory of ions travelling along the channel. When the presence of defects is sufficient, a part of the ions that initially travelled "channelled" will experience a process called "dechannelling" that will end with the collisions of ions with the host atoms. When the scattering angle of these collisions is big enough, it may end up causing backscattered ions. This increase in the number of backscattering ions due to the presence of defects is measured as an increase in the minimum yield at the bottom of the linear scan of the axial channel. Fig. 12 shows the linear scans around theta angle measured on the different samples. One can compare the yield at the minimum for the samples irradiated at different conditions. As can be observed, the yield at the minimum changes with the increase in damage. The pristine sample presents a minimum yield close to zero. It has a square-like shape, which is characteristic of good crystallinity. In the case of samples irradiated to 0.02 dpa/800 K (purple) and 0.02 dpa/290 K (green), even having the same implantation dose, show different yields at the minimum, being smaller for the 800 K case. The higher irradiation temperature results in fewer defects due to the higher recombination probability between defects since vacancies are mobile at these temperatures [33]. The same trend is observed for samples irradiated at 0.2 dpa, where the sample irradiated at 290 K shows the highest yield at the minimum, and the sample irradiated at 800 K is below the yield obtained on the samples irradiated at 290 K. The samples irradiated at 800 K show very similar yields. In addition, when looking at the spectra in Fig. 9, the signals are just at the surface very close to each other, and they start to deviate from each other, getting a higher yield for 0.2 dpa/800 K sample only at depths below 0.5 μm. This increase of the yield at the minimum is in agreement with the displacement damage observed by TEM, where the highest

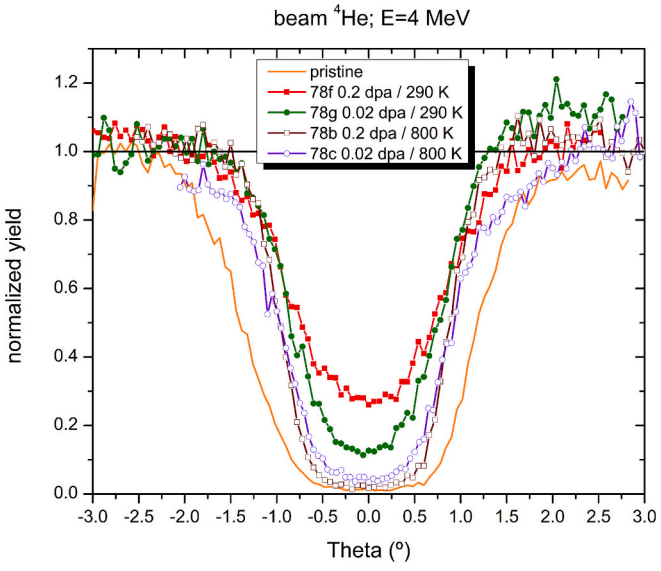

Fig. 12. Comparison of the ion yield for the linear scans along the axial channel <111> at 4 MeV ^{4}He energy for the pristine and the samples irradiated with W at two doses and two temperatures.

density of defects is observed on samples irradiated at 290 K to 0.2 dpa.

3.3. Positron annihilation lifetime spectroscopy

Positron annihilation lifetime measurements were performed by sandwiching the positrons source between a well-annealed reference and the W-irradiated sample of interest. The positron lifetime spectra are shown in Fig. 13 after subtracting source and background contributions and the 50 % of data produced by the reference. The single-component positron lifetime obtained in the reference samples (using two pieces of reference material) is shown as the black dashed line in the plot. All the spectra obtained in irradiated samples clearly show longer lifetime components than in the reference due to the irradiation-induced open-volume defects. Clearly, the effect of irradiation temperature is stronger than the effect of irradiation dose. The results of the detailed component analysis are shown in Table 5.

In the reference sample (single crystal sample annealed at 2325 K), one single component $\tau_B = 108$ ps was found. This is consistent with reported values of positron annihilation lifetime in defect-free tungsten (100–110 ps) [9]. Two-component analyses were performed on positron lifetime spectra measured in irradiated samples. Compared to the bulk value observed in the reference sample, the increase in the average positron lifetime indicates the accumulation of open-volume defects produced by self-ion irradiation. The analysed values of the longer component (τ_2) contain size information of irradiation-induced vacancy-type defects in the samples. Earlier studies report that the positron lifetime value in a mono-vacancy in tungsten ranges between 160 and 200 ps [9,33]. Here, the lowest value of $\tau_2 = 224 \pm 30$ ps in 78g (0.02 dpa/290 K) irradiated sample suggests vacancy defects larger than a mono-vacancy to be dominantly produced in the irradiated samples. The increase in the value of τ_2 up to 265(8) ps with improved uncertainty and relative increase of intensity (I_2) in sample 78f (0.2 dpa/290 K) compared to 78g (0.02 dpa/290 K) indicate an increase of average vacancy size with more irradiation damage accumulation. Based on theoretical calculations [9] the lifetime of 265 ps corresponds to small vacancy clusters of a size V_2 - V_4. For the high-temperature (800 K) irradiation process, the values of τ_2 increase above 400 ps regardless of the irradiation dose. The absolute values directly indicate that large vacancy clusters were produced with an estimated size of more than 25 missing atoms in the vacancy cluster, which implies a very different microstructure evolution mechanism when increasing the irradiation temperature from room temperature to 800 K. The reduced lifetime

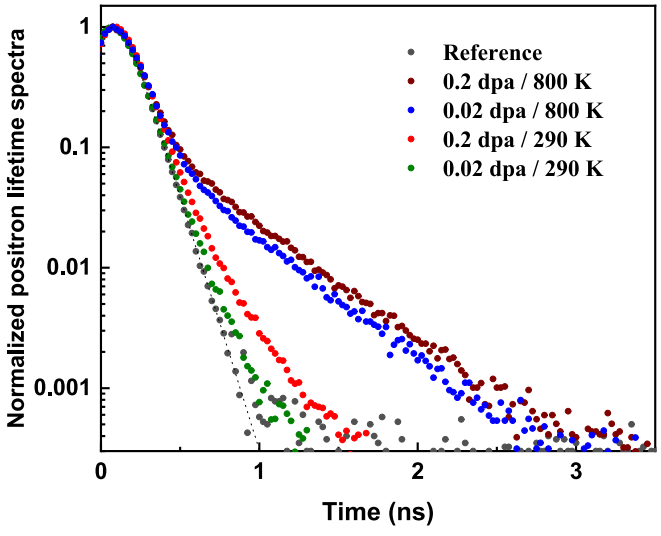

Fig. 13. Comparison of normalised positron lifetime spectra measured from well-annealed single crystal tungsten (111) and as-irradiated samples. All spectra have been modified with source and background subtraction.

Table 5
Single-component (average lifetime τ_{ave}) and two-component (lifetimes τ_1 and τ_2) exponential decay analysis of lifetime spectra measured in well-annealed and as-irradiated samples. (τ_{ave} (ps): τ_1 (ps) τ_2 (ps) I_2 (%)). The reduced chi-square values (χ^2_R) for each fitting are shown in the table.

Sample ID	Irradiation conditions	χ^2_R	τ_{ave} (ps)	τ_1 (ps)	τ_2 (ps)	I_2 (%)
2325 K_ref.	–	1.035	108	108 (1)	–	–
78g	0.02 dpa / 290 K	0.969	116	110 (2)	224 (30)	5.2 (2.5)
78f	0.2 dpa / 290 K	1.061	135	114 (1)	265 (8)	14.2 (1.3)
78c	0.02 dpa / 800 K	1.045	169	102 (1)	429 (4)	20.4 (0.4)
78b	0.2 dpa / 800 K	1.083	193	106 (1)	453 (3)	24.9 (0.3)

component (τ_1) analysed as 110–114 ps in 290 K irradiated samples and as 102–106 ps in 800 K irradiated samples is comparable with the bulk value (108 ps). The results are expected as 10.8 MeV self-ion irradiation produces damage in the first couple of micrometres in the near-surface layer, with roughly 75–80 % of the positrons expected to annihilate in the undamaged region deeper in the samples depends on the exponential stopping profile of energetic positrons emitted by the radioactive (β^+) source in tungsten. [31] This strongly suggests that the positron trapping is in saturation to the vacancy clusters in the damaged region in the samples 78c and 78b irradiated at 800 K.

3.4. Positron annihilation spectroscopy - Doppler broadening

The *S* parameters as a function of positron implantation energy (E) measured in 2325 K annealed and as-irradiated single crystals tungsten are shown in Fig. 14. The top *X*-axis shows the mean positron penetration depth in tungsten. All irradiated samples show higher *S* parameters, which indicates open-volume defect accumulation at the near-surface region (0 ~ 500 nm). A depth of 500 nm is the maximum depth detected by slow positrons. A clear dose effect is observed for the samples irradiated under the same temperature. Compared to the S parameters at a low dose (0.02 dpa), the relative increase at a high dose (0.2 dpa) indicates additional accumulation of vacancies either larger in size,

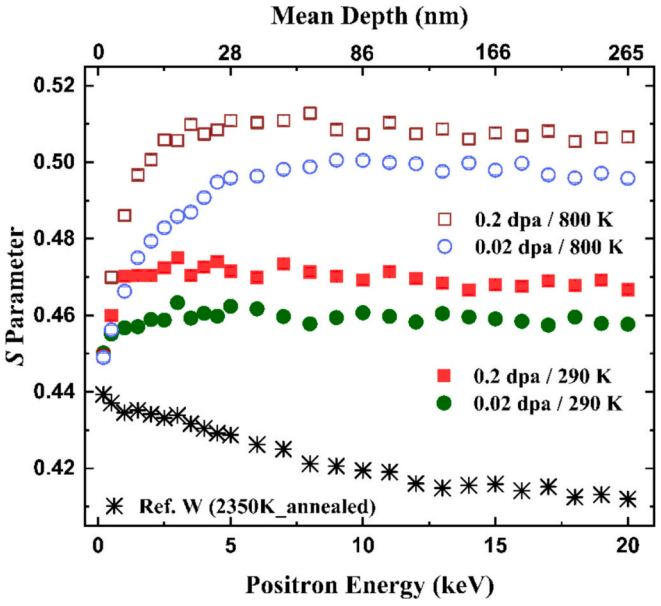

Fig. 14. *S* parameters measured as a function of implanted positron energy. The statistical errors are on the same scale as the data points.

concentration, or both. Similarly as in the case of lifetime experiments, the temperature effect on the *S* parameters is stronger than the dose effect.

We present (*S, W*) data points from selected depths in the *S*-*W* plot in Fig. 15. For the well-annealed reference sample, we only show data points from the highest positron implantation energies 18–20 keV, which shows the experimental (*S, W*) parameters closest to the values obtained for positron annihilation in defect-free tungsten. For the measurement data of irradiated samples, we extracted the (*S, W*) points measured by positrons with implantation energy of 5, 10, 15 and 20 keV. The relative (*S, W*) distribution and evolution with depth show that the vacancy defects are smaller in size but higher in concentration closer to the surface. This is evident from the behaviour of the (*S, W*) parameters.

As shown in Fig. 15, we have plotted several dashed lines ($L_1 - L_4$) to interpret the evolution of the size and concentration distribution of vacancy clusters with irradiation dose and temperature. All the lines originate from the bulk point of (*S, W*), and the relative change of line slope implies the growing of clusters in size [9,21,60]. The mono-vacancy ($S_{V1} = 0.447(4)$, $W_{V1} = 0.012(1)$) data point has been estimated by ratio the experimental data ($S_B = 0.412(1)$), $W_B = 0.0170(3)$) measured in well-annealed reference with normalization of ($S_{ref} = 1.0864$, $W_{ref} = 0.71$) [60]. The L_1 line represents the (*S, W*) parameter behaviour of positron annihilation in mono-vacancy since the calculated relative (S_{V1}, W_{V1}) parameter for mono-vacancy is well located on this line [21]. The location of (*S, W*) points on L_2 line represents small vacancy clusters with at most 2–4 missing atoms. The location of (*S, W*) points on L_3 and L_4 lines represent positron annihilation in larger vacancy clusters ($n > 25$, possibly up to 50 missing atoms) with respect to the positron lifetime analysis [60]. All these observations are in line with the positron lifetime data. The evolution with increasing probing depth (shown with arrows) indicates that the vacancy clusters are slightly larger deeper in the sample than close to the surface. At the same time, the concentration of these vacancy clusters is slightly lower deeper in the sample, as seen from the (*S, W*) drawn closer to the bulk reference point. For the 78g (0.02 dpa/290 K) sample, we determined mono-vacancy produced at the near-surface layer (~30 nm), while the variation of vacancy type has been observed in deeper layers. With the mean detection depth of 265 nm, small vacancy clusters ($2 < n < 4$) have been determined. For the 78f (0.2 dpa/290 K) sample, it turned out to be a di-vacancies accumulation close to the surface with a higher concentration than the low dose sample. There is less defect size variation in this sample from the surface to the bulk, and there small vacancy clusters $n = 4$ (V_4) prevail. From these observations, we can infer that the structure is similar to a low-dose sample, while small cluster accumulation takes place by increasing the irradiation dose. For the 800 K irradiated samples, the distribution of selected (*S, W*) points clearly shifted to larger vacancy cluster lines (L_3 and L_4) compared to the samples irradiated at 290 K, which is also consistent with the PALS results. For the 78c (0.02 dpa/800 K) sample, we speculate vacancy clusters of size about 25 (V_{25}) to be produced at the near-surface layer, while the increment of cluster size number has been determined in deeper layer. With the maximum mean detection depth of slow positrons, larger vacancy clusters of the size of around 50 could be estimated. For the 78b (0.2 dpa/800 K) sample, we also observe similar variation phenomenon that relatively smaller-sized vacancy clusters (~ V_{25}) are distributed in the near-surface layers, while the size of defect cluster increased up to ~ V_{50} in deeper layers due to the shifting of (*S, W*) points from L_3 to L_4. The upper-left shifting of (*S, W*) points of 78b compared to 78c suggests larger vacancy clusters formation due to the damage dose accumulation at 800 K. The fact that a concentration effect can be interpreted in the evolution suggests that the positron trapping is not fully in saturation. Hence, we conclude, comparing to the interpretation of the lifetime experiments, that the positron trapping in the 800 K samples is very close to the saturation limit. Assuming a value of $\mu_{V_N} = 1 \times 10^{16}\ s^{-1}$ for the trapping coefficient at large vacancy clusters and applying the atomic constant number $N_{at} = 6.34 \times 10^{28}$at./m^{-3} of tungsten, we can estimate the irradiation-induced vacancy cluster concentration as low-to-mid 10^{24} m^{-3} in the damaged region of the samples irradiated at 800 K. This corresponds to a mono-vacancy concentration in the 10^{25} m^{-3} range. We note that estimating the concentrations of the irradiation-induced vacancy defects is challenging as the positron lifetime experiments with fast positrons probe in large part the non-damaged region, and as the non-uniform defect profile seen in the (S, E) data prevents performing trustworthy analysis of the positron diffusion length in the irradiated samples. However, by combining the observations from both positron lifetime and the Doppler broadening data, we can make a tentative estimate of the vacancy defect concentration as described above in the 800 K irradiated samples. In the case of the samples irradiated at 290 K, lifetime data show a clearly smaller fraction of positrons annihilating at irradiation-induced vacancy defects than in the 800 K samples. This is most likely due to the shallower damage profile in the 290 K irradiated samples, as in the 800 K irradiated samples the mobility and clustering of the vacancy defects is expected to widen the distribution towards deeper in the sample [33,60]. The significant increase in the intensity I_2 of τ_2 when increasing the damage dose from 0.02 dpa to 0.2 dpa (78 g vs. 78f) suggests that in the 0.02 dpa sample the positron trapping is not in saturation in the damaged region. On the other hand, the fact that the (*S, W*) data in Fig. 15 are beyond the monovacancy point for the 0.02 dpa sample suggests that the trapping is not far from saturation to the small vacancy clusters. At these low damage levels at 290 K, we expect the concentration of the irradiation-induced vacancies to follow the damage dose roughly linearly due to the immobility of the vacancy defects. Assuming that for small vacancy clusters ($N < 10$) the positron trapping coefficient behaves as $\mu_N = N_{\mu_{V_1}}$, where $\mu_{V_1} = 10^{15}\ s^{-1}$, our tentative estimate for the concentration of the small vacancy clusters ($2 < n < 4$) is low 10^{24} m^{-3} in the 0.02 dpa sample and low-10^{25} m^{-3} in the 0.2 dpa sample.

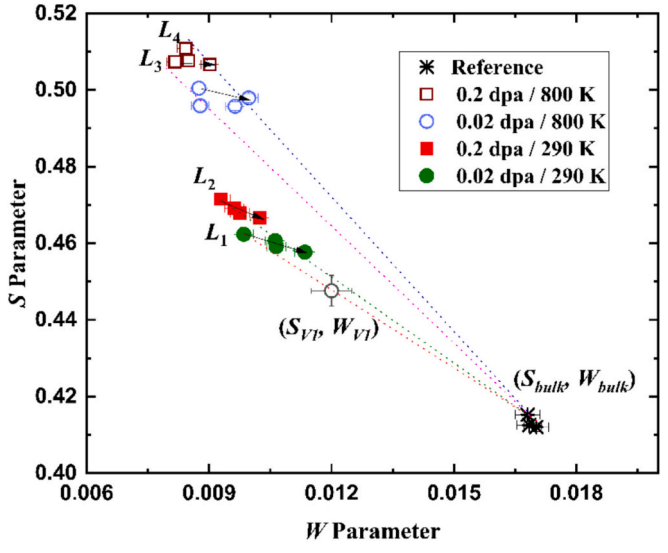

Fig. 15. The *S*-*W* plot of well-annealed and as-irradiated single crystal W (111) samples. For the reference sample, the (*S, W*) points with positron energy of (18–20) keV were extracted from well-annealed sample data, presented by cross marks. For the irradiated samples, the selected data points with positron energy of 5, 10, 15, and 20 keV have been shown to represent the irradiation-induced defect characteristics at different depth layers. The mono-vacancy point is obtained from Ref. [9, 60]. The dashed lines $L_1 - L_4$ indicate positron annihilation at different defect types: L_1 single vacancies, L_2 small vacancy clusters ($V_2 - V_4$), L_3 medium-size vacancy clusters, L_4 large vacancy clusters. The arrows indicate the variations of the measurement data from the near-surface to the bulk with the increment of detection energy.

3.5. Nuclear reaction analysis (NRA) deuterium depth profile measurements and thermal desorption spectroscopy (TDS)

The samples evaluated by PAS were afterwards exposed to D plasma and analysed by NRA using a ^{3}He beam at different energies to obtain quantitative D depth profiles (Fig. 16). D concentration of unirradiated W at the depth below 1.5 μm reaches values below 10^{-3} at. %, which is a typical level for non-irradiated W [5] under this D loading conditions and is close to the sensitivity limit. In contrast, for all W-irradiated samples, the amount of retained D is substantially increased in all samples due to the defects present in the microstructure. The increased D concentration is observed down to about 1.5 μm, which is in good agreement with the SRIM-calculated damage depth profile, also shown in Fig. 16 for the low damage dose. For the samples irradiated at 800 K, the increased D concentration extends down to 2 μm. The D concentration is the highest for the 78a (0.2 dpa/290 K) sample with 2 ± 0.08 at.% at the maximum. The sample 78h (0.02 dpa/290 K) shows about half that concentration with 0.98 ± 0.04 at.% at the maximum. The D concentrations for the samples damaged at 800 K are 0.38 ± 0.02 at.% for 78e (0.2 dpa/800 K) and 0.28 ± 0.03 at.% for 78d (0.02 dpa/800 K). We can conclude that higher irradiation temperature and lower damage dose result in smaller D concentration, indicating also fewer open volume defects.

In the D depth profiles, we observe a gradient of D concentration, indicating also a gradient of the defect concentration caused by heavy ion irradiation from the surface down to <0.5 μm. From the PAS analysis we learned about defect concentration and defect type down to 500 nm; in this damage region, the D concentrations are 1.85 ± 0.07 at. % for 0.2 dpa/290 K sample, 0.63 ± 0.05 at. % for 0.02 dpa/290 K sample, giving a ratio of three between the high and low damage dose. For the 800 K irradiated samples, the D concentration is 0.38 ± 0.02 at. % for 0.2 dpa and 0.13 ± 0.02 at. % for 0.02 dpa, resulting also in a ratio of three.

These samples, that were before analysed by PAS, loaded with deuterium plasma and analysed by NRA, were subjected to a TDS analysis using a heating ramp of 3 K/min. The measured deuterium desorption is shown in Fig. 16 for the four samples studied. The 0.2 dpa/290 K sample has two peaks, as has already been obtained for such highly damaged sample at 290 K [5], with the low-temperature peak at 570 K being higher than the high-temperature peak at 780 K. The 0.02 dpa/290 K sample also shows two peaks that are half as large as the 0.2 dpa/290 K sample, with a similar ratio between the low and the high-temperature peaks. However, both peaks are at a bit lower temperature as compared to the high damage dose sample, where low-temperature peak has a maximum at 540 K and the high-temperature peak at 755 K. It is interesting that in both cases at low and high dpa, the low temperature peaks are broad with a right shoulder at 630 K, especially pronounced for 0.02 dpa, indicating that there are probably two peaks combined. This is not the case for the 800 K samples, where the D desorption is lower compared to the 290 K samples, being in agreement with the NRA analysis and peaks look more symmetric. Moreover, contrary to the 290 K case, the low and the high-temperature peaks are of similar heights for the 800 K samples. The D desorption for the 0.2 dpa/800 K sample is higher than the D desorption of the 0.02 dpa/800 K sample, which is again in agreement with the NRA results. The desorption temperatures for the low-temperature peaks are at 545 K and at 530 K and the high-temperature peaks are at 780 K and 808 K, for samples irradiated at 800 K to 0.2 dpa and 0.02 dpa, respectively. During the TDS we do not expect evolution of the defects since in an detailed annealing study in 0.23 dpa /290 K irradiated tungsten pre-filled with deuterium we found that defects starts to evolve only after the deuterium is gone [61].

4. Discussion on comparison between different techniques

In the discussion section, we compare the results obtained by individual techniques, keeping in mind that each method offers distinct insight into the modified crystal structure. We will first compare the TEM results with the RBS-C measurements, as both are mainly sensitive to dislocation-type defects. The backscattering yield increases with damage dose and decreases with temperature. This agrees with the TEM results, where the largest and most extensive dislocation lines are observed on the 78f (0.2 dpa/290 K) sample, and then the dislocation features become smaller and less dense with lower damage dose and higher temperature (Figs. 6 and 7). Moreover, the relative disorder data as a function of probing beam energy show a positive slope for 0.2 dpa/290 K, indicating that extended defects are predominant defects, as confirmed by TEM analysis, where long dislocation lines have been observed for this sample. The relative disorder of the data obtained on other samples shows almost no slope, meaning that the predominant defect type would be a discontinuous type of defects. As demonstrated by TEM analysis in Figs. 6 and 7, small dislocation loops have been observed for the sample 78g (0.02 dpa/290 K), dislocation lines and black dots for the sample 78b (0.2 dpa/800 K) and loop and isolated lines for the sample 78c (0.02 dpa/800 K). This comparison allows us to conclude that the RBS-C and TEM results are consistent in reflecting the overall trend of defect formation in the samples.

Next, we compare PAS analysis with SEM and TEM. Positron annihilation spectroscopy (PAS) revealed varying concentrations of vacancies within the first 30 nm of the near-surface region. As reported in [7], the distribution of dislocation loops normalise at damage depths greater than 100 nm. These align with our SEM-ECP observations, where ECP patterns stabilised at voltages beyond 10 kV, penetrating to a depth of 0.17 μm, and with defect observations made by BF-STEM analysis, where the thickness of the defect depleted zone near the surface for

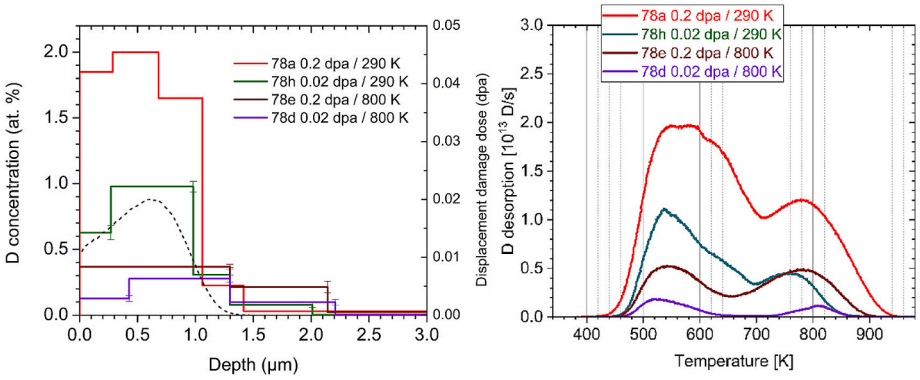

Fig. 16. (left) D concentration depth profiles as obtained on the different W-irradiated W (111) SC samples. SRIM-calculated damage depth profile is shown by a dashed line with Y right scale for low damage dose samples. (right) Deuterium desorption spectra measured for these samples as a function of the temperature measured on the sample. A heating rate of 3 K/min was applied.

dislocation-type defects was measured in the order of tens of nanometers. As the irradiation dose increases for W samples irradiated at room temperature, the primary interstitial-type defects transform from dislocation loops ($\leq$ 0.1 dpa) into dislocation lines (0.1–0.15 dpa), and eventually forming dislocation networks ($\geq$ 0.15 dpa). Finally, a dynamic equilibrium of defects is achieved at doses $\geq$0.2 dpa, characterised by a stable microstructure where networks and loops coexist [7]. Vacancy clusters in W typically evolve into dislocation loops when they reach a critical size of about 20 to 50 vacancies [60,62]. However, this can vary based on irradiation conditions, such as dose rate and temperature, as well as specific microstructural environments. Dislocation loops in tungsten typically form as ⟨100⟩ or ⟨111⟩ loops. At higher temperatures, the mobility of vacancies increases, which can lead to the formation of larger vacancy clusters before they evolve into dislocation loops. Conversely, at lower temperatures, smaller clusters might be sufficient to trigger the dislocation loop formation. Higher irradiation doses lead to a higher concentration of vacancies, which can cause smaller vacancy clusters to reach the critical size more quickly, leading to earlier dislocation loops forming in the irradiation process.

Further, we can compare cluster sizes obtained by PAS and TEM. With PAS analysis we can determine if voids of a detectable size should appear in TEM, as TEM can identify vacancy clusters above a certain size threshold, at which point they are classified as voids. According to [63,64], a void measuring 1.51 nm in diameter corresponds to approx. 113 vacancies. From Ref. [64] and the table within, and using this relationship between void size (calculation of the void volume) and vacancy clusters, a 0.94 nm void would equate to a cluster of about 27 vacancies. For the samples irradiated at 290 K, the vacancy clusters are relatively small, up to about 4 vacancies (V_4). In contrast to the 800 K samples, where PAS detected clusters of around 25 vacancies (V_{25}) at 0.02 dpa, increasing to 50 vacancies (V_{50}) at 0.2 dpa; implying a void size of approximately 0.92 nm for low-dose irradiation and 1.16 nm for high-dose irradiation. In the TEM analysis of the sample irradiated at 0.2 dpa/800 K, we observed voids ranging in size from 0.25 nm to 1 nm (mean ferret of 0.44 nm corresponding to V_4), with a density of 5.46 $\times$ 10^{24} m^{-3}, of the same order of magnitude as observed with PAS. Moreover, the vacancy cluster size detected by PAS agrees with the void size observed by Hu et al. [21] observing voids between 0.97 and 1.13 nm, depending on the sample purity.

The PAS results were validated by the D retention study using NRA analysis. The implantation at 290 K led to higher D retention than implantation at 800 K due to the influence of vacancy mobility. PAS analysis showed that at 0.02 dpa at 290 K, mono-vacancy (V_1) and vacancy clusters ($V_{2<n<4}$) form in the near-surface region. However, as the damage increases to 0.2 dpa, mono-vacancies begin to coalesce, forming larger vacancy clusters (V_2 to V_5). The molecular dynamics calculations [65] agree well with the PAS results, showing dominant production of single and di-vacancies. The D concentration at 0.02 dpa (0.63 at.%) is half lower than the concentration in the 0.2 dpa / 290 K sample (1.85 at. %). At 800 K, hydrogen isotopes will be trapped in large vacancy clusters ($\geq V_{25}$). For the 800 K, the D retention decreases as compared to 290 K irradiation, reaching 0.38 $\pm$ 0.02 at.% for the sample damaged to 0.2 dpa and 0.28 $\pm$ 0.03 at.% at 0.02 dpa damaged sample. With the increase in the irradiation dose, the vacancy cluster size increase from V_{25} to V_{50}, with concentrations low-to-mid 10^{24} m^{-3}. D retention in damaged W increases proportionally with irradiation dose, with D retention nearly twice larger as the dose increases from 0.02 to 0.2 dpa. This trend is consistent for the 290 K and 800 K irradiated samples. Further macroscopic rate equation modelling is needed to obtain the detrapping energies of D in defects and concentrations of the individual defects from the TDS spectra, which is out of the scope of this paper.

To correlate the D concentrations with the defect concentrations obtained by PAS (Table 5), one needs to know how many D atoms can be contained in vacancy clusters of a certain size. In this comparison, the main assumption is that hydrogen isotopes are trapped in tungsten at open-volume defects, which are vacancies and vacancy clusters. Density functional theory showed that a single vacancy can contain up to 6 deuterium atoms at low temperatures [66], whereas vacancy clusters can contain even more deuterium atoms, as shown in [67]. The number of D that can be stored in the defect steadily increases with the size of the cluster and is dependent on the loading temperature. If we make a simple calculation for the sample irradiated at 0.02 dpa / 290 K where di-vacancies are dominant, PAS gives a density of low 10^{24} m^{-3}. Assuming these divacancies concentration as single vacancies, multiplying the density by two, we get density for single vacancies of mid 10^{24} m^{-3}. Dividing the volume concentration by W density of 6.34 $\times$ 10^{28} m^{-3}, this result in a vacancy atomic concentration of 10^{-2} at. %. Multiplying this concentration with 6, assuming 6 D atoms fill a vacancy, one gets a D concentration of 0.05 at.%. In the NRA D depth profile study, we obtained 0.63 at. % in the PAS-DB detection region. This means we are missing one order of magnitude of defect density from PAS. Still, one needs to consider that there is a distribution of vacancy clusters inside the sample with different number of vacancies, and PAS gives only the concentration for the defect that is mostly populated. Namely, when larger vacancy clusters are present in the sample, the positrons are more attracted to larger vacancy clusters that are most populated. This implies that, given an equal concentration of small and large vacancy clusters, the relative sensitivity to detect small vacancy clusters decreases. This likely contributes to the observed underestimation of D concentration based on vacancy cluster concentration measurements in PAS-DB. Further information about the concentrations for individual vacancy clusters in the samples could be extracted from D depth profiles and the TDS spectra using macroscopic rate equation modelling, which is out of the scope of this paper.

5. Conclusions

This study aims to compare multiple analytical techniques to investigate how the influence of exposure temperature and dose affect defect formation, and to correlate insights gathered from each technique. A method for advanced surface preparation of tungsten (111) single crystal was developed, which consists of stepwise vibrational polishing and additional high-temperature annealing to achieve a defect-free microstructure. The electron channelling pattern (ECP) in SEM, which serves as a stereogram of the crystal lattice projected along the optical axis, was effectively used for assessing surface quality, verifying successful irradiation (e.g., detecting possible shadowing), ensuring precise azimuthal orientation of the samples during oriented sample preparation, and qualitatively estimating the amount of introduced crystal structure defects.

Self-ion irradiation of W(111) at temperatures of 290 K and 800 K was successfully performed to deliberately introduce various types of defects into the microstructure. Both undamaged and damaged samples were analysed using multiple analytical techniques to characterise the types and amounts of defects, including electron microscopy, multi-energy RBC-C, positron annihilation lifetime and Doppler broadening spectroscopy (PALS and PAS-DP), nuclear reaction analysis (NRA) for deuterium (D) depth profiling and thermal desorption spectroscopy (TDS) for D trapping kinetics. This is the first time these methods have been applied to tungsten single crystals prepared under the same irradiation conditions for two irradiation doses of 0.02 dpa and 0.2 dpa and two temperatures of 290 K and 800 K.

TEM and RBS-C provided insights into dislocation-type defects, while PAS and NRA revealed information on open-volume defects, vacancies, and vacancy clusters. There is a strong agreement between these techniques, offering complementary data. For instance, PAS revealed the dominant size of vacancy clusters across samples, while NRA quantified the total defect sites that trap hydrogen, and TDS offered D detrapping kinetics, which could then be linked to specific defects. This combined information is essential for predicting hydrogen trapping energy in defects and supports rate equation modelling from ab initio data. Such data directly validate theoretical models, like molecular

dynamics simulations, in predicting defect formation, including both dislocation and vacancy types.

CRediT authorship contribution statement

J. Zavašnik: Writing – review & editing, Writing – original draft, Investigation, Formal analysis, Data curation, Conceptualization. **A. Šestan:** Writing – review & editing, Investigation, Formal analysis, Data curation. **T. Schwarz-Selinger:** Writing – review & editing, Writing – original draft, Methodology, Investigation, Funding acquisition, Formal analysis, Data curation, Conceptualization. **K. Hunger:** Writing – review & editing, Methodology, Formal analysis. **E. Lu:** Writing – review & editing, Writing – original draft, Methodology, Formal analysis. **F. Tuomisto:** Writing – review & editing, Writing – original draft, Methodology, Formal analysis, Data curation. **K. Nordlund:** Formal analysis, Data curation. **E. Punzón-Quijorna:** Writing – review & editing, Writing – original draft, Methodology, Formal analysis, Data curation. **M. Kelemen:** Formal analysis, Data curation. **J. Predrag:** Formal analysis, Data curation. **M.L. Crespillo:** Writing – review & editing, Methodology, Formal analysis. **G. García López:** Writing – review & editing, Investigation, Formal analysis, Data curation. **P. Zhang:** Investigation, Formal analysis. **X. Cao:** Investigation, Formal analysis. **S. Markelj:** Writing – review & editing, Writing – original draft, Supervision, Resources, Project administration, Investigation, Funding acquisition, Formal analysis, Data curation, Conceptualization.

Declaration of competing interest

The authors declare that they have no known competing financial interests or personal relationships that could have appeared to influence the work reported in this paper.

Acknowledgments

This work has been carried out within the framework of the EUROfusion Consortium, funded by the European Union via the Euratom Research and Training Programme (Grant Agreement No. 101052200 — EUROfusion). Views and opinions expressed are however those of the author(s) only and do not necessarily reflect those of the European Union or the European Commission. Neither the European Union nor the European Commission can be held responsible for them. The authors acknowledge the support from the Slovenian Research and Innovation Agency, research core funding No. P2-0405, P1-0417, and research projects No. J2-3038, J2-4440, and support from The Centro de Microanalisis de Materiales (CMAM)-Universidad Autónoma de Madrid, for the beam time proposal (Multi-energy and multi-axial channelling study of induced damaged in W(111) crystals for DeHydroC project) with code STD039/22, and its technical staff for their contribution to the operation of the accelerator. Part of this work was supported by the Max-Planck partner group *High Performance Materials*. The authors acknowledge the financial support from the Research Council of Finland No. 349602, 354777.

Appendix A. Supplementary data

Supplementary data to this article can be found online at https://doi.org/10.1016/j.matchar.2025.115050.

Data availability

The authors confirm that the data supporting the findings of this study are available within the article and its supplementary information file materials.

References

[1] B. Wielunska, M. Mayer, T. Schwarz-Selinger, A.E. Sand, W. Jacob, Deuterium retention in tungsten irradiated by different ions, Nucl. Fusion 60 (2020) 096002, https://doi.org/10.1088/1741-4326/AB9A65.
[2] O.V. Ogorodnikova, V. Gann, Simulation of neutron-induced damage in tungsten by irradiation with energetic self-ions, J. Nucl. Mater. 460 (2015) 60–71, https://doi.org/10.1016/J.JNUCMAT.2015.02.004.
[3] S.M. Myers, P.M. Richards, W.R. Wampler, F. Besenbacher, Ion-beam studies of hydrogen-metal interactions, J. Nucl. Mater. 165 (1989) 9–64, https://doi.org/10.1016/0022-3115(89)90502-3.
[4] K. Schmid, T. Schwarz-Selinger, R. Arredondo, A. Theodorou, T. Pomella Lobo, Implications of T loss in first wall armor and structural materials on T-self-sufficiency in future burning fusion devices, Nucl. Fusion 64 (2024) 076056, https://doi.org/10.1088/1741-4326/AD52A7.
[5] T. Schwarz-Selinger, A critical review of experiments on deuterium retention in displacement-damaged tungsten as function of damaging dose, Mater. Res. Express 10 (2023) 102002, https://doi.org/10.1088/2053-1591/ACFDF8.
[6] S. Markelj, T. Schwarz-Selinger, M. Pečovnik, A. Založnik, M. Kelemen, I. Čadež, J. Bauer, P. Pelicon, W. Chromiński, L. Ciupinski, Displacement damage stabilization by hydrogen presence under simultaneous W ion damage and D ion exposure, Nucl. Fusion 59 (2019) 086050, https://doi.org/10.1088/1741-4326/AB2261.
[7] S. Wang, W. Guo, T. Schwarz-Selinger, Y. Yuan, L. Ge, L. Cheng, X. Zhang, X. Cao, E. Fu, G.H. Lu, Dynamic equilibrium of displacement damage defects in heavy-ion irradiated tungsten, Acta Mater. 244 (2023) 118578, https://doi.org/10.1016/J.ACTAMAT.2022.118578.
[8] A. Hollingsworth, M.F. Barthe, M.Y. Lavrentiev, P.M. Derlet, S.L. Dudarev, D. R. Mason, Z. Hu, P. Desgardin, J. Hess, S. Davies, B. Thomas, H. Salter, E.F. J. Shelton, K. Heinola, K. Mizohata, A. De Backer, A. Baron-Wiechec, I. Jepu, Y. Zayachuk, A. Widdowson, E. Meslin, A. Morellec, Comparative study of deuterium retention and vacancy content of self-ion irradiated tungsten, J. Nucl. Mater. 558 (2022) 153373, https://doi.org/10.1016/J.JNUCMAT.2021.153373.
[9] Q. Yang, Z. Hu, I. Makkonen, P. Desgardin, W. Egger, M.F. Barthe, P. Olsson, A combined experimental and theoretical study of small and large vacancy clusters in tungsten, J. Nucl. Mater. 571 (2022) 154019, https://doi.org/10.1016/J.JNUCMAT.2022.154019.
[10] P.M. Derlet, S.L. Dudarev, Microscopic structure of a heavily irradiated material, Phys. Rev. Mater. 4 (2020) 023605, https://doi.org/10.1103/PHYSREVMATERIALS.4.023605/FIGURES/19/MEDIUM.
[11] D.R. Mason, F. Granberg, M. Boleininger, T. Schwarz-Selinger, K. Nordlund, S. L. Dudarev, Parameter-free quantitative simulation of high-dose microstructure and hydrogen retention in ion-irradiated tungsten, Phys. Rev. Mater. 5 (2021) 095403, https://doi.org/10.1103/PHYSREVMATERIALS.5.095403/FIGURES/8/MEDIUM.
[12] R. Delaporte-Mathurin, R. Chochoy, J. Mougenot, Y. Charles, E.A. Hodille, C. Grisolia, 3D effects on hydrogen transport in ITER-like monoblocks, Nucl. Fusion 64 (2023) 026003, https://doi.org/10.1088/1741-4326/AD1019.
[13] E.A. Hodille, E. Bernard, S. Markelj, J. Mougenot, C.S. Becquart, R. Bisson, C. Grisolia, Estimation of the tritium retention in ITER tungsten divertor target using macroscopic rate equations simulations, Phys. Scr. 2017 (2017) 014033, https://doi.org/10.1088/1402-4896/AA8787.
[14] T. Schwarz-Selinger, Deuterium retention in MeV self-implanted tungsten: influence of damaging dose rate, Nucl. Mater. Energy 12 (2017) 683–688, https://doi.org/10.1016/J.NME.2017.02.003.
[15] W. Chrominski, L. Ciupinski, P. Bazarnik, S. Markelj, T. Schwarz-Selinger, TEM investigation of the influence of dose rate on radiation damage and deuterium retention in tungsten, Mater. Charact. 154 (2019) 1–6, https://doi.org/10.1016/J.MATCHAR.2019.05.028.
[16] O.V. Ogorodnikova, Y. Gasparyan, V. Efimov, J. Grzonka Ciupiński, Annealing of radiation-induced damage in tungsten under and after irradiation with 20 MeV self-ions, J. Nucl. Mater. 451 (2014) 379–386, https://doi.org/10.1016/J.JNUCMAT.2014.04.011.
[17] S. Markelj, T. Schwarz-Selinger, A. Založnik, M. Kelemen, P. Vavpetič, P. Pelicon, E. Hodille, C. Grisolia, Deuterium retention in tungsten simultaneously damaged by high energy W ions and loaded by D atoms, Nucl. Mater. Energy 12 (2017) 169–174, https://doi.org/10.1016/J.NME.2016.11.010.
[18] X. Yi, M.L. Jenkins, M.A. Kirk, Z. Zhou, S.G. Roberts, In-situ TEM studies of 150 keV W+ ion irradiated W and W-alloys: damage production and microstructural evolution, Acta Mater. 112 (2016) 105–120, https://doi.org/10.1016/J.ACTAMAT.2016.03.051.
[19] X. Yi, M.L. Jenkins, K. Hattar, P.D. Edmondson, S.G. Roberts, Characterisation of radiation damage in W and W-based alloys from 2 MeV self-ion near-bulk implantations, Acta Mater. 92 (2015) 163–177, https://doi.org/10.1016/J.ACTAMAT.2015.04.015.
[20] X. Yi, M.L. Jenkins, M. Briceno, S.G. Roberts, Z. Zhou, M.A. Kirk, In situ study of self-ion irradiation damage in W and W–5Re at 500°C, Philos. Mag. 93 (2013) 1715–1738, https://doi.org/10.1080/14786435.2012.754110.
[21] Z. Hu, P. Desgardin, C. Genevois, J. Joseph, B. Décamps, R. Schäublin, M.F. Barthe, Effect of purity on the vacancy defects induced in self–irradiated tungsten: a combination of PAS and TEM, J. Nucl. Mater. 556 (2021) 153175, https://doi.org/10.1016/J.JNUCMAT.2021.153175.
[22] W. Jiang, Y. Zhu, L. Zhang, D.J. Edwards, N.R. Overman, G. Nandipati, W. Setyawan, C.H. Henager, R.J. Kurtz, Dose rate effects on damage accumulation and void growth in self-ion irradiated tungsten, J. Nucl. Mater. 550 (2021) 152905, https://doi.org/10.1016/J.JNUCMAT.2021.152905.

[23] L.C. Feldman, W. Mayer, S.T. Picraux, Materials Analysis by Ion Channeling : Submicron Crystallography, Academic Press, 1983. ISBN 978-0-12-252680-0.
[24] M. Boleininger, D.R. Mason, A.E. Sand, S.L. Dudarev, Microstructure of a heavily irradiated metal exposed to a spectrum of atomic recoils, Sci. Rep. 13 (1) (2023) 1–11, https://doi.org/10.1038/s41598-022-27087-w.
[25] F. Granberg, D.R. Mason, J. Byggmästar, Effect of simulation technique on the high-dose damage in tungsten, Comput. Mater. Sci. 217 (2023) 111902, https://doi.org/10.1016/J.COMMATSCI.2022.111902.
[26] S. Markelj, X. Jin, F. Djurabekova, J. Zavašnik, E. Punzón-Quijorna, T.S.- Selinger, M.L. Crespillo, G.G. López, F. Granberg, E. Lu, K. Nordlund, A. Šestan, M. Kelemen, Unveiling the radiation-induced defect production and damage evolution in tungsten using multi-energy Rutherford backscattering spectroscopy in channeling configuration, Acta Mater. 263 (2024) 119499, https://doi.org/10.1016/J.ACTAMAT.2023.119499.
[27] S. Zhang, K. Nordlund, F. Djurabekova, Y. Zhang, G. Velisa, T.S. Wang, Simulation of Rutherford backscattering spectrometry from arbitrary atom structures, Phys. Rev. E 94 (2016) 043319, https://doi.org/10.1103/PHYSREVE.94.043319/FIGURES/11/MEDIUM.
[28] X. Jin, F. Djurabekova, M. Sequeira, K. Lorenz, K. Nordlund, Effect of lattice voids on Rutherford backscattering dechanneling in tungsten, J. Phys. D. Appl. Phys. 56 (2023) 065303, https://doi.org/10.1088/1361-6463/ACAD12.
[29] S. Markelj, E. Punzón-Quijorna, M. Kelemen, T. Schwarz-Selinger, R. Heller, X. Jin, F. Djurabekova, E. Lu, J. Predrag, First study of the location of deuterium in displacement-damaged tungsten by nuclear reaction analysis in channeling configuration, Nucl. Mater. Energy 39 (2024) 101630, https://doi.org/10.1016/J.NME.2024.101630.
[30] M. Pečovnik, E.A. Hodille, T. Schwarz-Selinger, C. Grisolia, S. Markelj, New rate equation model to describe the stabilization of displacement damage by hydrogen atoms during ion irradiation in tungsten, Nucl. Fusion 60 (2020) 036024, https://doi.org/10.1088/1741-4326/AB680F.
[31] F. Tuomisto, I. Makkonen, Defect identification in semiconductors with positron annihilation: experiment and theory, Rev. Mod. Phys. 85 (2013) 1583–1631, https://doi.org/10.1103/REVMODPHYS.85.1583/FIGURES/27/MEDIUM.
[32] F.A. Selim, Positron annihilation spectroscopy of defects in nuclear and irradiated materials- a review, Mater. Charact. 174 (2021) 110952, https://doi.org/10.1016/J.MATCHAR.2021.110952.
[33] J. Heikinheimo, K. Mizohata, J. Räisänen, T. Ahlgren, P. Jalkanen, A. Lahtinen, N. Catarino, E. Alves, F. Tuomisto, Direct observation of mono-vacancy and self-interstitial recovery in tungsten, APL Mater. 7 (2019), https://doi.org/10.1063/1.5082150/150766.
[34] R. Bes, A. Vancraeyenest, PALSRaM: a three-detector positron annihilation lifetime spectrometer for γ-emitting radioactive materials, Nucl. Instrum. Meth. Phys. Res. A. 1052 (2023) 168265, https://doi.org/10.1016/J.NIMA.2023.168265.
[35] A. Redondo-Cubero, M.J.G. Borge, N. Gordillo, P.C. Gutiérrez, J. Olivares, R. Pérez Casero, M.D. Ynsa, Current status and future developments of the ion beam facility at the centre of micro-analysis of materials in Madrid, Eur. Phys. J. Plus 136 (2) (2021) 1–16, https://doi.org/10.1140/EPJP/S13360-021-01085-9.
[36] B. Wielunska, M. Mayer, T. Schwarz-Selinger, U. Von Toussaint, J. Bauer, Cross section data for the D(3He,p)4He nuclear reaction from 0.25 to 6 MeV, Nucl. Inst. Methods Phys. Res. B 371 (2016) 41–45, https://doi.org/10.1016/J.NIMB.2015.09.049.
[37] K. Schmid, U. Von Toussaint, Statistically sound evaluation of trace element depth profiles by ion beam analysis, Nucl. Inst. Methods Phys. Res. B 281 (2012) 64–71, https://doi.org/10.1016/J.NIMB.2012.03.024.
[38] M. Mayer, SIMNRA User's Guide, Max-Planck-Institut Für Plasmaphysik, Garching Bei München, 1997. https://mam.home.ipp.mpg.de/Report%20IPP%209-113.pdf (accessed October 23, 2024).
[39] E. Salançon, T. Dürbeck, T. Schwarz-Selinger, F. Genoese, W. Jacob, Redeposition of amorphous hydrogenated carbon films during thermal decomposition, J. Nucl. Mater. 376 (2008) 160–168, https://doi.org/10.1016/J.JNUCMAT.2008.02.070.
[40] T. Schwarz-Selinger, J. Bauer, S. Elgeti, S. Markelj, Influence of the presence of deuterium on displacement damage in tungsten, Nucl. Mater. Energy 17 (2018) 228–234, https://doi.org/10.1016/J.NME.2018.10.005.
[41] D.C. Joy, D.E. Newbury, D.L. Davidson, Electron channeling patterns in the scanning electron microscope, J. Appl. Phys. 53 (1982) R81–R122, https://doi.org/10.1063/1.331668.
[42] A. Založnik, Interaction of Atomic Hydrogen with Materials Used for Plasma-Facing Wall in Fusion Devices, Doctoral Thesis, https://repozitorij.uni-lj.si/IzpisGradiva.php?id=97441, 2016.
[43] D. Drouin, A.R. Couture, D. Joly, X. Tastet, V. Aimez, R. Gauvin, CASINO V2.42 - a fast and easy-to-use modeling tool for scanning electron microscopy and microanalysis users, Scanning 29 (2007) 92–101, https://doi.org/10.1002/sca.20000.
[44] Y.N. Picard, R. Kamaladasa, M. De Graef, N.T. Nuhfer, W.J. Mershon, T. Owens, L. Sedlacek, F. Lopour, Future prospects for defect and strain analysis in the SEM via Electron channeling, Micros Today 20 (2012) 12–16, https://doi.org/10.1017/S1551929512000077.
[45] A. Šestan, L. Sreekala, S. Markelj, M. Kelemen, J. Zavašnik, C.H. Liebscher, G. Dehm, T. Hickel, M. Čeh, S. Novak, P. Jenuš, Non-uniform he bubble formation in W/W2C composite: experimental and ab-initio study, Acta Mater. 226 (2022) 117608, https://doi.org/10.1016/J.ACTAMAT.2021.117608.
[46] K. Nordlund, F. Djurabekova, G. Hobler, Large fraction of crystal directions leads to ion channeling, Phys. Rev. B 94 (2016) 214109, https://doi.org/10.1103/PHYSREVB.94.214109/FIGURES/18/MEDIUM.
[47] J.F. Ziegler, M.D. Ziegler, J.P. Biersack, SRIM – the stopping and range of ions in matter (2010), Nucl. Inst. Methods Phys. Res. B 268 (2010) 1818–1823, https://doi.org/10.1016/J.NIMB.2010.02.091.
[48] O.V. Ciupiński, T. Ogorodnikova, M. Płociński, M. Andrzejczuk, M. Rasiński, K. J. Mayer, Kurzydłowski, TEM observations of radiation damage in tungsten irradiated by 20 MeV W ions, Nucl. Inst. Methods Phys. Res. B 317 (2013) 159–164, https://doi.org/10.1016/J.NIMB.2013.03.022.
[49] S. Zaefferer, N.N. Elhami, Theory and application of electron channelling contrast imaging under controlled diffraction conditions, Acta Mater. 75 (2014) 20–50, https://doi.org/10.1016/J.ACTAMAT.2014.04.018.
[50] R.D. Kerns, S. Balachandran, A.H. Hunter, M.A. Crimp, Ultra-high spatial resolution selected area electron channeling patterns, Ultramicroscopy 210 (2020) 112915, https://doi.org/10.1016/J.ULTRAMIC.2019.112915.
[51] S.L. Dudarev, P. Rez, M.J. Whelan, Theory of electron backscattering from crystals, Phys. Rev. B 51 (1995) 3397, https://doi.org/10.1103/PhysRevB.51.3397.
[52] S. Yamasaki, Observation and measurement using the Electron channeling pattern function, Tech. Mag. Electron Microsc. Anal. Instrum. 19 (2023) 1–8. https://www.hitachi-hightech.com/file/global/pdf/sinews/si_report/130215.pdf (accessed November 7, 2023).
[53] B. Wielunska, T. Płociński, T. Schwarz-Selinger, M. Mayer, W. Jacob, L. Ciupiński, Dislocation structure of tungsten irradiated by medium to high-mass ions, Nucl. Fusion 62 (2022) 096003, https://doi.org/10.1088/1741-4326/AC75FF.
[54] Y. Meng, X. Ju, X. Yang, The measurement of the dislocation density using TEM, Mater. Charact. 175 (2021) 111065, https://doi.org/10.1016/J.MATCHAR.2021.111065.
[55] S. Hasanzadeh, R. Schäublin, B. Décamps, V. Rousson, E. Autissier, M.F. Barthe, C. Hébert, Three-dimensional scanning transmission electron microscopy of dislocation loops in tungsten, Micron 113 (2018) 24–33, https://doi.org/10.1016/J.MICRON.2018.05.010.
[56] F. Ferroni, X. Yi, K. Arakawa, S.P. Fitzgerald, P.D. Edmondson, S.G. Roberts, High temperature annealing of ion irradiated tungsten, Acta Mater. 90 (2015) 380–393, https://doi.org/10.1016/J.ACTAMAT.2015.01.067.
[57] X. Meng, J. Zhao, An evaluation of Ar ion milling in TEM sample preparation by energy-filtered TEM technique, Vacuum 222 (2024) 112980, https://doi.org/10.1016/J.VACUUM.2024.112980.
[58] Y. Zhou, G. Velişa, S. San, M.L. Crespillo, Z. Fan, H. Bei, W.J. Weber, P. Xiu, L. Wang, F. Tuomisto, W.Y. Ching, Y. Zhang, Role of chemical disorder on radiation-induced defect production and damage evolution in NiFeCoCr, J. Nucl. Mater. 565 (2022) 153689, https://doi.org/10.1016/J.JNUCMAT.2022.153689.
[59] W. Kan Chu, J.W. Mayer, M.-A. Nicolet, Backscattering Spectrometry, Academic Press, 1978. ISBN 978-0-12-173850-1.
[60] M. Zibrov, W. Egger, J. Heikinheimo, M. Mayer, F. Tuomisto, Vacancy cluster growth and thermal recovery in hydrogen-irradiated tungsten, J. Nucl. Mater. 531 (2020) 152017, https://doi.org/10.1016/J.JNUCMAT.2020.152017.
[61] M. Pečovnik, S. Markelj, M. Kelemen, T. Schwarz-Selinger, Effect of D on the evolution of radiation damage in W during high temperature annealing, Nucl. Fusion 60 (2020) 106028, https://doi.org/10.1088/1741-4326/ABAFF6.
[62] A.E. Sand, S.L. Dudarev, K. Nordlund, High-energy collision cascades in tungsten: dislocation loops structure and clustering scaling laws, Europhys. Lett. 103 (2013) 46003, https://doi.org/10.1209/0295-5075/103/46003.
[63] J. Fikar, R. Schäublin, D.R. Mason, D. Nguyen-Manh, Nano-sized prismatic vacancy dislocation loops and vacancy clusters in tungsten, Nucl. Mater. Energy 16 (2018) 60–65, https://doi.org/10.1016/J.NME.2018.06.011.
[64] J. Fikar, R. Schäublin, Stability of small vacancy clusters in tungsten by molecular dynamics, Nucl. Inst. Methods Phys. Res. B 464 (2020) 56–59, https://doi.org/10.1016/J.NIMB.2019.11.044.
[65] F. Granberg, J. Byggmästar, K. Nordlund, Molecular dynamics simulations of high-dose damage production and defect evolution in tungsten, J. Nucl. Mater. 556 (2021) 153158, https://doi.org/10.1016/J.JNUCMAT.2021.153158.
[66] K. Heinola, T. Ahlgren, K. Nordlund, J. Keinonen, Hydrogen interaction with point defects in tungsten, Phys. Rev. B. Condens Matter. Mater. Phys. 82 (2010) 094102, https://doi.org/10.1103/PHYSREVB.82.094102/FIGURES/3/MEDIUM.
[67] J. Hou, X.S. Kong, X. Wu, J. Song, C.S. Liu, Predictive model of hydrogen trapping and bubbling in nanovoids in bcc metals, Nat. Mater. 18 (8) (2019) 833–839, https://doi.org/10.1038/s41563-019-0422-4.